UNIVERSITY OF TECHNOLOGY, SYDNEY

SCHOOL OF MECHANICAL ENGINEERING

SOME TURBULENCE CHARACTERISTICS OF THE CONVECTIVELY MIXED LAYERS OVER RUGGED AND HOMOGENEOUS TERRAIN

B.P. Huynh
C.E. Coulman
T.R. Turner

TECHNICAL REPORT
UTS/ME 103

November 1988

SOME TURBULENCE CHARACTERISTICS OF THE CONVECTIVELY MIXED LAYERS OVER RUGGED AND HOMOGENEOUS TERRAIN[+]

B.P. HUYNH[*]
School of Mechanical Engineering,
University of Technology, Sydney, NSW, Australia

C.E. COULMAN[*]
Université de Nice
Departement d' Astrophysique
Nice, Cedes, France

T.R. TURNER[**]
Division of Mathematics
University of New Brunswick,
Fredericton, New Brunswick, Canada

[+] This work was initiated and a large part of it was completed while all the three authors were with CSIRO (Commonwealth Scientific Industrial Research Organisation).

[*] Formerly at: Division of Atmospheric Research, CSIRO, Epping, NSW, Australia.

[**] Formerly at: Division of Mathematics and Statistics, CSIRO, Lindfield, NSW, Australia.

ABSTRACT

Turbulence characteristics obtained by using an aircraft of the convectively mixed layers over rugged and homogenous terrain are presented, and their differences are sought. Apart from the statistics related to the mixing ratio q, there does not seem to be marked difference between the two sets of data. This lack of difference is attributed to the degree of ruggedness of the terrain and the dominant wind direction. The behaviour of some statistics related to q is attributed to the entrainment effect of the unstable layer of the moist, cool air above the mixed layer.

1. INTRODUCTION

Although the investigation of the turbulence structure in the atmospheric boundary layer over homogeneous terrain has had a long history, it is only recently that similar work over rugged terrain has been carried out (Panofsky et al., 1982; Kaimal et al., 1982; Druilhet et al., 1983a). Considering that most terrain is rugged to some extent, the investigation of the atmospheric boundary layer over complex terrain is somewhat overdue. In this paper, we report some turbulence characteristics in the boundary layers in convective conditions. The data were collected by an instrumented aircraft over both homogeneous and rugged terrain. A parallel presentation of data will be made so that any dissimilarity, or lack of it, between homogeneous and rugged terrain cases can be identified. We also present our data in the background of some published results by other workers.

2. THE OBSERVATION PROGRAM

2.1 Generalities

The observation program was carried out on board the CSIRO research aircraft, an F-27. The aircraft is fitted with a 6.5 m long nose boom, and the instruments for measuring air motion and temperatures are fitted on the front part of this boom, relatively free from the aircraft-induced effects. Table 1 shows further details about the instruments used.

A total of four days of observation relevant to this report was carried out consisting of two days over rugged terrain with 32 runs and two days over relatively homogeneous terrain with 19 runs. These four days are designated as C12, C13, M23 and M29 as shown in Table 2. The days and times chosen for observation - usually between mid-days and early afternoons - are such that fairly steady convective conditions are ensured to be dominant. Table 2 shows some more details about the observation program, meteorological and ground conditions.

Each aircraft "production" run is done at a constant altitude and in a straight line of about 15 km long, lasting about 3 minutes. The altitudes are, however, varied among the runs, so that the boundary layer mid-region of between $0.04z_i$ and $0.8z_i$ are covered, where z_i is the mixed-layer height. Spiral soundings over the centre parts of the investigated regions are carried out immediately before the first run and after the last run of the observation "day", to determine the instantaneous values of z_i. The values of z_i at intermediate times are then interpolated from these two readings. For M29, however, due to the short time involved, only one sounding is made at the end of the series of runs, and the z_i value thus determined is used for all the runs.

To obtain z_i's from the spiral soundings, plots of the virtual potential temperature Θ_v and mixing ratio Q versus altitude are produced, and z_i's can be fairly accurately determined as the top levels of the well-mixed layers. Figure 1a shows a typical such plot, with the two corresponding soundings used for C12. It is noted, however, that Figure 1a shows the characteristic features for all but one of the aircraft spiral soundings, namely that immediately on top of the mixed layer is the inversion layer with stable stratification and composed of dry air. The one exception is the afternoon sounding for day M23, shown in Figure 1b, which was done immediately after the last "run" in that day. This figure shows that there is an unstable layer composed of moist, cool air, residing on top of the warmer mixed layer. The effect of this instability will be discussed later when we deal with the covariance between θ and q, the fluctuations of potential temperature and of vapour mixing ratio respectively.

2.2 Description of Sites

The rugged-terrain site is centred over Callide reservoir (24°22′S, 150°38′E) in Queensland, Australia; and the homogeneous site is over farm land (29°53′S, 149°27′E) to the South West of Moree in New South Wales, Australia.

The Callide site is at the western foothills of the Callide mountain range which is running North West - South East, with peaks rising to a maximum of about 900 m in the vicinity of the site. Callide reservoir is at an altitude of 210 m AMSL; and all "heights above ground level" at the Callide site are measured relative to this altitude. To the West of the reservoir is the Bannana-Cooper mountain range, composed of more isolated hills with peaks rising to a maximum of about 500 m, and running parallel to the Callide range. The valley between the ranges, which is about 20 km wide near the reservoir, has the lowest altitude contour of about 140 m AMSL. The vegetation covering the area is typically scattered forest in the valley and on the Bannana-Cooper ranges, and medium to dense forest on the Callide range. Figure 2a shows a coarse contour map of the region and Figure 2b shows a coarse view of the Callide site, respectively.

The Moree site is typically flat, extensive farm land at various stages of cultivation and harvesting. Isolated patches of forest can also be seen but there is no significant land mark in the region. The average altitude is 180 m AMSL. Some more details about the ground conditions can be seen in Table 2.

2.3 Data Processing

Measurements are collected in situ on magnetic tapes at the rates of 100 samples/s for "fast" data, and 5 for "slow" data. Because the various instruments are mounted at different locations, and have different response time delays, care has been taken to ensure that all relevant signals are synchronised. The fast data are then numerically filtered via a Fast Fourier Transform (FFT) scheme to give a maximum frequency of 10 Hz. Most of the slow data are, however, averaged to give 2-second averages. Table 1 gives some further details about the variables involved. The 10 Hz time series are then used to obtain various statistics, after being linearly detrended. The computers involved are the ROLM for data collection, the Cyber 76 for processing and the VAX 11/750 for statistical analysis.

As shown in Table 2, each "run" lasts about 3 minutes. Assuming Taylor's hypothesis of frozen turbulence, and with a typical aircraft air speed of 80 m/s, this gives maximum wave lengths of about 14 km. The number of useful data points per time series is, however, only about 3300, corresponding to 165s of data sampling in the mid-section of the time series.

For computations involving spectra, like those for the peak wavelengths of the vertical velocity fluctuations or the dissipation rate of kinetic energy, a FFT scheme is used.

The computation of co-variances and variances are, however, performed by eddy correlation method. The variance of air speed fluctuation v is treated differently, however. In this case, due to the resonant effect in the 3 m long plastic tube connecting the Pitot tube and the transducer-amplifier unit, there is a significant lifting at the high frequency end of the response curve of the probe. Therefore, the variance of v is calculated from

$$\overline{v^2} = \int_{f_{min}}^{f_{max}} S_v(f).df$$

where f is the frequency and S_v is the corrected spectra of v. The corrected variance is, however, only about 11% lower than the uncorrected one at the high frequency end.

For temperatures, on the other hand, there are some attenuations in the probes' frequency response at frequencies above 3Hz. The errors involved are, however, small, and the temperature variances are expected to be low by less than 5% for Callide data, and less than 2% for Moree data. Assuming there is no significant phase shifts between the relevant paramaters, the heat fluxes and temperature-mixing ratio co-variances are also expected to be fairly accurate.

3. RESULTS

3.1 Scaling Factors

In a steady convective mixed layer, it has been amply shown (Deardorff, 1970; Kaimal et al., 1976; Wyngaard et al., 1978; Guillemet et al., 1983; etc.) that the appropriate scaling factors are (for notation, see Appendix)

$$\begin{aligned} & z_i && \theta = \overline{(w\theta)}_o / w_* \\ & w_* = (g\overline{(w\theta)}_o \, z_i/\theta)^{1/3} && q_* = \overline{(wq)}_o / w_* \end{aligned} \qquad (1)$$

We adopt (1) in this report. Here, the ground fluxes $(w\theta)_o$ and $(wq)_o$ are obtained by extrapolation from the values obtained at higher levels.

In the following, we show our results, often on the background of published results by other workers. Extensive comparison is made against Druilhet et al's data, therefore, a note should be made: their data were collected in a more rugged terrain, under stronger wind condition.

3.2 Co-variances and Correlation Coefficients

The vertical profiles of the normalised co-variance $\overline{w\theta}/\overline{(w\theta)}_o$ representing normalised sensible heat flux are shown in Figure 3. There seems to be no discernible difference between the rugged terrain profile and that over homogeneous terrain. Our values are similar to the AMTEX data of Wyngaard et al. (1978), and the Ashchurch - Minnesota data of Caughey and Palmer (1979), but somewhat lower than those obtained by Lenschow (1974), or Druilhet et al. (1983a) for homogeneous terrain condition. Our ruged terrain data also lack the irregularities shown in Druilhet et al.'s rugged terrain data.

The correlation coefficients $r_{w\theta}$ between w and θ are shown in Figure 4. Like the normalised sensible heat flux, there is no recognisable difference between the cases for rugged and smooth terrain. Also, our data seem to show a tendency for $r_{w\theta}$ to stay constant up to $z/z_i \doteq 0.1$ only, compared to 0.3 as suggested by Druilhet et al. (1983a)'s results. Our $r_{w\theta}$ value at the ground is, however, similar to the homogeneous terrain ground value of Druilhet et al., namely about 0.6.

Figures 3 and 4 also show that, from our data, the zero heat flux occurs at the level of $z/z_i \doteq 0.7$. This level is comparable to that obtained by Wyngaard et al. (0.67), but lower than those of Lenschow (0.87), or Druilhet et al. (0.81).

Profiles of the normalised moisture flux $\overline{wq}/(\overline{wq})_o$ are shown in Figure 5. Despite large scattering, the data still show recognisable decreasing trends with height. The trends are perhaps similar for the rugged and smooth terrain, but steeper than that from AMTEX data (Wyngaard et al., 1978). In Figure 6, it can be seen that the correlation coefficient r_{wq} also shows similar trends over rugged and smooth terrain, but with rugged terrain values slightly higher. Our data do not show the constancy of r_{wq} with height, as found by Druilhet et al. (1983). Also, here the projected ground values of r_{wq} are somewhat higher (0.4 for smooth terrain, and 0.5 for rugged terrain) than those shown in Druilhet et al.'s paper.

Figures 7 and 8 show the vertical profiles of the normalised co-variance $\overline{\theta q}/\theta_* q_*$ and the correlation coefficient $r_{\theta q}$. The smooth terrain data of M23 show strong anti-correlation between θ and q for most of the upper part of the mixed layer. In fact, positive correlation occurs only for $z/z_i < 0.2$. This value is much smaller than the 0.5 obtained from Druilhet et al. (1983a)'s observations, or the 0.6 obtained by Deardorff's (1974) numerical simulation. It should be noted, as shown in Table 2, that on the day M23, the observational site was covered with extensive cumulus cloud, and there were even some short showers. The result is that, as revealed in the afternoon sounding for day M23 shown in Figure 1b, there is an unstable layer composed of moist, cool air residing on top of the warmer mixed layer. It is the entrainment of this moist, cool layer of air into the mixed layer, that causes such deep penetration and results in negative values of $r_{\theta q}$ to be observed down to such low levels. This mechanism is more effective and different from the "normal" entrainment where the dry, warm air in the stable inversion layer is entrained into the cooler mixed layer. This later mechanism is found in Druilhet et al.'s and Deardorff's works, and in our data over rugged terrain.

Over rugged terrain, the values of $\overline{\theta q}/(\theta_* q_*)$ seem to collapse well, and stay positive, although small, for most of the lower part of the mixed layer. The cross-over point to negative values occur probably at about 0.7 z_i. This rather high level, when compared with homogeneous terrain data of Druilhet et al. (0.5 z_i) and Deardorff's simulation (0.6 z_i), is thought of to be due to the advective effects of the underlying topography, which preserve the long wavelength components of the convective structures associated with rising warm, moist air from the ground, and limit the entrainment effect to the top 30% of the mixed layer. The correlation coefficient $r_{\theta q}$, on the other hand, seems to stay fairly constant at about 0.55, up to $z/z_i \doteq 0.3$, then decreases linearly with height. This is in contrast to Druilhet et al.'s data, which show $r_{\theta q}$ over rugged terrain to be small, negative, and nearly constant for the whole of the mixed layer ($r_{\theta q} = -0.1$).

3.3 Variances

Figure 9 shows the vertical profiles of the normalised variance of the vertical velocity fluctuation $\overline{w^2}/w_*^2$.

There does not seem to be any significant difference between the rugged terrain and the homogeneous terrain data; except in the upper part of the mixed layer, where the only few data points available seem to suggest that the homogeneous terrain values are smaller. Overall $\overline{w^2}/w_*^2$ increases quickly with height near the ground, reaches a maximum value of about 0.5 at $z/z_i \doteq 0.5$, before starting to decrease again. The homogeneous terrain data follow well Wyngaard et al. (1971)'s free convection prediction of $1.8\,(z/z_i)^{2/3}$, up to $z/z_i \doteq 0.1$. In the middle part of the mixed layer, all data seem to agree with Willis and Deardorff (1974)'s laboratory average results, as presented by Caughey and Palmer (1979), whose data are, however, lower than ours.

Profiles of the normalised variance of potential temperature, $\overline{\theta^2}/\theta_*^2$, are shown in Figure 10. Again, rugged terrain and homogeneous terrain data do not show any substantial difference, except that the rugged terrain values are perhaps slightly larger than the homogeneous terrain ones for $z < 0.4z_i$. Compared to the data obtained by Caughey and Palmer (1979), and the aircraft data assembled by Willis and Deardorff (1974) (not shown), our data agree well in the surface layer ($z/z_i < 0.1$), but become slightly larger at levels higher up. In the surface layer the data follow the $(z/z_i)^{-2/3}$ law, but with a coefficient of about 1.5 instead of 1.8 as predicted by the free convection formulation (Wyngaard et al., 1971). The minimum value for $\overline{\theta^2}/\theta_*^2$ is about 0.3, and occurs at $z/z_i \doteq 0.5$, the same level as the maximum value of $\overline{w^2}/w_*^2$.

Figure 11 shows that the variance of the mixing ratio q does not seem to follow a simple scaling scheme, as used here. An attempt at the interfacial scaling scheme similar to the one proposed by Tuzet et al. (1983) did not seem to help very much in collapsing the data either perhaps because of the uncertainties in the values of $\delta\Theta/\delta z$ and $\delta Q/\delta z$ immediately above z_i in some data. However, the smooth terrain data M23 show that entrainment effect can be felt as far down as $z/z_i \doteq 0.2$, consistent with the θ-q co-variance results shown in Figure 7. The C13 and M29 sets of data, taken together, seem to be the only ones which have some similarity with the free convection formulation of Snedman-Högstrom (1973). The C12 data, however, do not show significant variation with height.

Since in most of the data collection runs, the aircraft flight paths are either at small angles with, or perpendicular to the wind directions, therefore the fluctuations v_a in its airspeed approximately correspond to the longitudinal or transversal fluctuations in the wind speed, u and v, respectively. Thus, Figure 12 shows the normalised variance $\overline{v_a^2}/w_*^2$. Again, there does not seem to be any significant difference between the rugged terrain and homogeneous terrain. The M23 homogeneous terrain data, however, seem to indicate some slight decrease with height. Taking all data together, however, then $\overline{v_a^2}/w_*^2$ seems to be constant with height, fluctuating about 0.55. Caughey and Palmer (1979) also obtained similar distribution of $\overline{u^2}/u_*^2$ and $\overline{v^2}/w_*^2$ with height, but on the average their data are smaller, being at 0.4.

3.4 Peak Wavelengths

The peak wavelengths are defined here as the wavelengths corresponding to the maximum values of $kS_x(k)$ in the x variable. Here, Taylor's frozen turbulence hypothesis has been assumed, so that $k = f/V_a$ where f is the frequency measured in the aircraft's frame of reference, and V_a is the aircraft air speed.

The peak wavelengths $(\lambda_m)_w$ from the spectra of the vertical velocity fluctuation w are shown in Figure 13. Again, there does not seem to be any substantial difference betweem homogeneous terrain and ruged terrain data, except that the latter show more scattering due to the interaction of turbulence with the underlying terrain. Despite the scarcity and large scattering of the rugged terrain data in the upper region, the tendency for $(\lambda_m)_w$ to decrease with height above $z/z_i \doteq 0.5$ is still recognisable. Our data therefore seem to be similar to those obtained by Caughey and Palmer, and the lower part $(z/z_i < 0.5)$ of Kaimal et al.'s (1976) results. Druilhet et al. (1983a) also obtained similar results over homogeneous terrain; however, our data do not seem to show smaller values over rugged terrain as theirs. Figure 13 shows that the maximum value of $(\lambda_m)_w$ is about 1.5 z_i and occurs at $z/z_i \doteq 0.5$.

For the potential temperature fluctuation θ, the peak wavelengths $(\lambda_m)_\theta$ are more difficult to obtain, due to the low frequency variations from run to run. However, approximate peaks in the $kS_\theta(k)$ plots can still be identified to give $(\lambda_m)_\theta$ as shown in Figure 14. Despite large scattering, it still can be seen that $(\lambda_m)_\theta$ increases quickly with height in the surface layer, then approaches a steady value of about 2z_i for $z/z_i > 0.5$. There does not seem to be a tendency for $(\lambda_m)_\theta$ to decrease at higher levels, as (λ_m) w does. This is to be compared with Kaimal et al.'s (1976) data, which show that as z approaches 0.1 z_i, $(\lambda_m)_\theta$ approaches the characteristic wavelength 1.5 z_i, same as the maximum value of $(\lambda_m)_w$. Thus, the vertical profile of $(\lambda_m)_\theta$ from our data changes more gradually than that of Kaimal et al. (see Figure 14).

Again, there does not seem to be any systematic difference between the rugged and homogeneous terrain data shown here, except that the rugged terrain data show more scattering.

3.5 Dissipation Rates

The rates of dissipation of turbulent kinetic energy ϵ, temperature variance N_θ, and mixing ratio variance N_q, are estimated from the inertial subrange of one dimensional spectra of fluctuations in vertical velocity, temperature and mixing ratio respectively. Assuming frozen turbulence hypothesis, the useful relations are

$$f^{5/3}.S_w(f) = \frac{4}{3}\alpha_u \left(\frac{V_a}{2\pi}\right)^{2/3}\epsilon^{2/3} \quad ; \quad \alpha_u = 0.5$$

$$f^{5/3}.S_\theta(f) = \alpha_\theta \left(\frac{V_a}{2\pi}\right)^{2/3}\epsilon^{-1/3} N_\theta \; ; \; \alpha_\theta = 0.8$$

$$f^{5/3}.S_q(f) = \alpha_q \left(\frac{V_a}{2\pi}\right)^{2/3}\epsilon^{-1/3}N_q \; ; \; \alpha_q = 0.8$$

Here, we adopt the numerical values of α_u, α_θ and α_q as from Druilhet et al. (1983b).

Figure 15 shows the vertical distribution of normalised ϵ, defined here as $\epsilon_* = \epsilon.z_i/w_*^3$. The rugged and homogeneous terrain data do not show any significant difference. Our data show a rapid decrease of ϵ_* with height, up to $z/z_i \doteq 0.2$, then stay almost constant at the value of about 0.24, right up to $z \doteq 0.8\ z_i$ which is the highest level in our set of data. In this way, Guillemet et al. (1983), Caughey and Palmer (1979) have obtained similarly constant results, but with larger values. For the bulk of the mid-section of the mixed layer, Guillemet et al.'s data are between 0.35 and 0.65, while Caughey and Palmer's data are between about 0.51 and 0.77, as shown in Figure 15. On the other hand, Druilhet et al. (1983a)'s homogeneous terrain data show that ϵ_* decreases at a much larger, and constant, slope with height. Below $z \doteq 0.7z_i$, their rugged terrain data also show similar, but somewhat weaker behaviour.

The vertical profile of the normalised dissipation rate of the temperature variance, defined here as $(N_\theta)_* = N_\theta z_i/w_*\theta_*^2$, is shown in Figure 16. Here the rugged terrain values are slightly larger than those over homogeneous terrain, for z below about 0.4 z_i; but overall, there is no substantial difference between the two sets of data. This is similar to the behaviour of $\overline{\theta^2}/\theta_*^2$ shown in Figure 10. Our data seem to follow closely the profile of data obtained by Caughey and Palmer (1979), except that the present $(N_\theta)_*$ are smaller, as shown in Figure 16. Also, in the lower levels ($z/z_i < 0.5$), our data seem to agree fairly well with the $(z/z_i)^{-4/3}$ law predicted under local free convection similarity hypothesis (Wyngaard, 1973). The dashed line in Figure 16 represents the relation:

$$(N_\theta)_* = A_\theta(z/z_i)^{-4/3}$$

where the constant $A_\theta = 0.4$ is estimated by eye-fitting the observational points. The present value of A_θ is somewhat smaller than the 0.55 value given by Guillemet et al. (1983).

Figure 17 shows the vertical profile of normalised dissipation rate of the mixing ratio variance, $(N_q)_* = N_q z_i/w_* q_*^2$. Compared with the profiles of q^2/q_*^2 shown in Figure 11, some similarity can be seen. The entrainment effect in the M23 set of data can still be seen to be effective as far down as $z = 0.2\ z_i$; and the C13 set of data, together with the data points below $z = 0.1\ z_i$ in the homogeneous terrain cases show the free convection behaviour of $A_q(z/z_i)^{-4/3}$. However our value of $A_q = 0.5$, obtained by eye-fitting the data points, is smaller than the 0.9 value given by Guillemet et al. (1983).

4. CONCLUDING REMARKS

Overall, our data do not show any marked difference in the turbulence statistics between homogeneous and rugged terrain, except for those related to the mixing ratio q as shown in Figures 7, 8, 11, and to a milder degree in Figure 6. The difference between homogeneous and rugged terrain data shown in these figures are, however, believed to be due to the entrainment effects from the layers above z_i, and thus dependent more on the conditions in these layers, than on the underlying terrain. In this way, our results are very different from those obtained by Druilhet et al. (1983a), who have shown substantial variations between data collected over homogeneous and rugged terrains. One way to explain the differences between our results and Druilhet et al.'s is that because on the two days where the C12 and C13 sets of data were collected, the wind is light and is mainly from the South-West to West-South West (see Table 2). Since to the West and South of the observational site, as shown in Figures 2a and 2b, the terrain is somewhat less rugged than the one in Druilhet et al.'s paper (see Noilham et al. (1983) for a description of their experimental site), the terrain-induced turbulence in our data is not strong enough to cause any large deviation from the homogeneous terrain cases, except for the larger scattering in the data points. Thus, our data show that results from homogeneous terrain experiments are still valid for terrain with some degree of ruggedness, at least to the extent encountered in this report.

APPENDIX

NOTATION

Θ	[K]	mean potential temperature of the mixed layer
θ	[K]	potential temperature fluctuation
w	[m/s]	vertical velocity fluctuation
v	[m/s]	aircraft airspeed fluctuation, along the flight direction
z	[m]	height above ground level
z_i	[m]	height above ground level of the mixed layer
q	[g/kg]	water vapour mixing ratio
g	[m/s^2]	gravitational constant
S_x		spectra of variable x
f	[Hz]	frequency
k	[cycle/m]	wave number
r_{xy}		correlation coefficient between variable x and y
$(\lambda_m)_x$	[m/cycle]	maximum wavelength of variable x, i.e. the wavelength at the maximum value of $S_x(f)$

SUBSRIPTS

$_o$	at ground surface
$_*$	for normalising factors
a	for aircraft

LIST OF FIGURES

Figure 1a

Typical vertical profiles of virtual potential temperature Θ_v and mixing ratio Q obtained from aircraft spiral soundings. The heights of the mixed layer z_i can be readily read off as shown above. The two curves on the left are Θ_v, and Q curves are shown on the right. The soundings are made above Callide reservoir at 11.40 (Θ_v-11.40, Q-11.40) and 14.37 (Θ_v-14.37, Q-14.37).

Figure 1b

Vertical profiles of virtual potential temperature Θ_v and mixing ratio Q of the "exceptional" day M23.

Figure 2a

A contour map of the Callide region. The heavy-lined rectangle corresponds to the Callide site shown in Figure 2b.

Figure 2b

A coarse view of the Callide site, corresponding to the heavy-lined rectangle in Figure 2a. Here the origin O is set at the mean sea level point of 24°23′13"S 150°30′00"E. ============ : projected ground track. ——————-——— : approximate boundary of the Callide reservoir.

Figure 3

Normalised kinematic heat flux $h_* = \overline{w\theta}/\overline{(w\theta)}_o$ versus normalised height $z_* = z/z_i$ above ground level. Rugged terrain data: +, C12 (see Table 2 for observation symbols); x, C13. Homogeneous terrain data: ●, M23 ; θ, M29; 0, from Wyngaard et al. (1978); o: from Caughey and Palmer (1979);-----, Deardorff (1972)'s presentation of Lenschow's (1970) aircraft results.

Figure 4

$r_{w\theta}$ versus z/z_i. Symbols are same in Figure 3.

Figure 5

Normalised moisture flux $\overline{wq}/\overline{(wq)}_o$ versus z/z_i. Symbols are same as in Figure 3.

Figure 6

r_{wq} versus z/z_i. Symbols are same as in Figure 3.

Figure 7

Normalised co-variance $\overline{\theta q}/(\theta_* q_*)$ versus z/z_i. Symbols are same as in Figure 3.

Figure 8

$r_{\theta q}$ versus z/z_i . Symbols are same as in Figure 3.

Figure 9

Normalised variance of the vertical velocity fluctuation $\overline{w^2}/w_*^2$ versus z/z_i. ————————: free convection formulation for the surface layer, $\overline{w^2}/w_*^2 = 1.8\ (z/z_i)^{2/3}$, by Wyngaard et al. (1971); — — — — — — —: The average of the S_1 and S_2 cases in Willis and Deardorff's (1974) laboratory results, as presented by Caughey and Palmer (1979). Other symbols are same as in Figure 3.

Figure 10

Normalised variance of the potential temperature $\overline{\theta^2}/\theta_*^2$ versus z/z_i.————————: free convection formulation, $\overline{\theta^2}/\theta_*^2 = 1.8(z/z_i)^{-2/3}$, by Wyngaard et al. (1971); — — — — — — — —: The S_1 case in Willis and Deardorff's (1974) laboratory results. Other symbols are same as in Figure 3.

Figure 11

Normalised variance of the mixing ratio $\overline{q^2}/q_*^2$ versus z/z_i; ——·——·——: free convection formula $\overline{q^2}/q_*^2 = 2.59(z/z_i)^{-2/3}$, by Smedman-Högström (1973). Other symbols are same as in Figure 3.

Figure 12

Normalised variance of the aircraft fluctuation $\overline{v_a^2}/w_*^2$ versus z/z_i.— — — — — — —: the average of the S_1 and S_2 cases in Willis and Deardorff's (1974) laboratory results, as presented by Caughey and Palmer (1979). Other symbols are same as in Figure 3.

Figure 13

Normalised peak wavelength $(\lambda_m)_w/z_i$ of w spectra, versus z/z_i. ————————: free convection formulation $(\lambda_m)_w/z_i = 5.9\ z/z_i$, $z < 0.1z_i$, by Kaimal et al. (1976);——·——·—— ; Kaimal et al.'s results for region $0.1 < z/z_i < 1.0$. Other symbols are same as in Figure 3.

Figure 14

Normalised peak wavelength $(\ _m)_\theta/z_i$ of θ spectra versus z/z_i; ————————: curve fitting data by eyes;——·——·—— : Kaimal et al.'s results. Other symbols are same as in Figure 3.

Figure 15

Normalised dissipation rate of turbulent kinetic energy $\epsilon z_i/w_*^3$ versus z/z_i. Symbols are same as in Figure 3.

Figure 16

Normalised dissipation rate of temperature variance, $(N_\theta)_* = N_\theta z_i / w_* \theta_*^2$ versus z/z_i. ———————— : Guillemet et al.'s smooth terrain formulation $(N_\theta)_* = 0.55\ (z/z_i)^{-4/3}$; —·———·——: curve fitting data by eyes $(N_\theta)_* = 0.4\ (z/z_i)^{-4/3}$. Other symbols are same as in Figure 3.

Figure 17

Normalised dissipation rate of mixing ratio variance $(N_q)_* = N_q z_i / w_* q_*^2$ versus z/z_i. ———————— : Guillemet et al.'s smooth terrain formulation $(N_q)_* = 0.9\ (z/z_i)^{-4/3}$;——·———·——: curve fitting data by eyes $(N_q)_* = 0.5\ (z/z_i)^{-4/3}$. Other symbols are same as in Figure 3.

REFERENCES

Caughey, S.J. and Palmer, S.G. (1979), "Some aspects of turbulence structure through the depth of the convective layer", Quart. J. Roy. Meteor. Soc., 105, 811-827.

Deardorff, J.W. (1970), "Convective velocity and temperature scales for the unstable planetary boundary layer and for Rayleigh convection", J. Atmos. Sci., 27, 1211-1213.

Deardorff, J.W. (1974), "Three-dimensional numerical study of turbulence in an entraining mixed layer", Bound.-Layer Meteor., 7, 199-226.

Druilhet, A. et al. (1983a), "Étude expérimentale de la couche limite au-desus d' un relief modéré proche d' une chaîne de montague", Bound.-Layer Meteor., 25, 3-16.

Druilhet, A. et al. (1983b), "Experimental studies of the turbulence structure parameters of the convective boundary layer", J. Climate Appl. Meteor., 22, 594-608.

Guillemet, B. et al. (1983), "Molecular dissipation of turbulent fluctuations in the convective mixed layer. Part 1: Height variations of dissipation rates", Bound.-Layer Meteor., 27, 141-162.

Kaimal, J.C. et al. (1976), "Turbulence structure in the convective boundary layer", J. Atmos. Sci., 33, 2152-2169.

Kaimall, J.C. et al. (1982), "Spectral characteristics of the convective boundary layer over uneven terrain", J. Atmos. Sci., 39, 1098-1114.

Lenschow, D.H. (1974), "Model of the height variation of the turbulence kinetic energy budget in the unstable planetary boundary layer", J. Atmos. Sci., 31, 465-474.

Noilham, J. et al. (1983), "Étude expérimentale de la couche limite au-dessus d' un relief modéré proche d'une chaîne de montagne", Bound.-Layer Meteor., 24, 395-414.

Panofsky, H.A. et al. (1982), "Spectra of velocity components over complex terrain", Quart. J. Roy. Meteor. Soc., 108, 215-230.

Smedman-Högström, A.S. (1973), "Temperature and humidity spectra in the atmospheric surface layer", Bound.-Layer Meteor., 3, 329-347.

Tuzet, A. et al. (1983), "Echelles interfaciales des fluctuations de température et d'humidité dans la couche de mélange convective", J. de Recherches Atmosphériques, 17, 185-197.

Willis, G.E. and Deardorff, J.W. (1974), "A laboratory model of the unstable planetary boundary layer", J. Atmos. Sci., 31, 1297-1307.

Wyngaard, J.C. (1973), "On surface layer turbulence, in Workshop on Micrometeorology, D.A. Haugen, ed., Amer. Meteor. Soc., Boston, Mass., USA, 101-149.

Wyngaard, J.C. et al. (1971), "Local free convection, similarity, and the budgets of shear stress and heat flux", J. Atmos. Sci., 28, 1171-1182.

Wyngaard, J.C. et al. (1978), "The temperature-humidity covariance budget in the convective boundary layer", J. Atmos. Sci., 35, 47-58.

TABLE 1

Quantities	Methods of Measurement	Sampling Rates (Samples/second)	Maximum Frequencies retained after numerical filtering (fast response) or averaging (slow response) (Hz)
Reference Temperatures			
- Dry bulb	"Rosemount" Platinum element, Ø 1.3 mm	5	0.25
- Wet bulb	"	5	0.25
Fast-response Temperatures			
- Dry bulb	Nickel wire, Ø 12.5 µm	100	10
- Wet bulb	Nickel wire, Ø 25.0 µm	100	10
Mixing ratio	Derived numerically from measurements of dry and wet bulb temperatures	5 and 100	0.25 and 10
Air vertical velocity fluctuation (artificially de-meaned)	Two angle-of-attack fixed vanes, fitted with "Micro-measurement" strain gauges	100	10
Air speed	Pitot tube, connected by a 3 m plastic tube to a "Statham" pressure transducer-amplifier unit	100	0.25 and 10
Pressures (for heights)			
- Static	"Kistler" unit, model 314A	5	0.25
- Dynamic	"Kistler: unit, model 314D	100	10
Height above ground level	Radiometer	5	0.25
Surface temperature (not used here)		5	2.5

TABLE 2

Observation Symbols	Location and Date	Starting time of first and last runs	Number of runs	Mean aircraft air-speed	Duration of each run	Flight direction	Wind speed	Wind direction	Flight direction relative to wind direction	Number of Projected ground tracks	Cloud conditions	Ground conditions	Remarks
				m/s	min		m/s						
C12 Rugged terrain	Callide, 12/7/81	12.08 & 14.23	16	85.5	3	90°, 270°	1 -2.5; mainly 1.5-2	190°-280°; mainly 210°-240°	slanting angle	1	clear sky	See text	
C13 Rugged terrain	Callide 13/7/81	11.25 & 13.29	16	85.5	3	90°, 270°	2 - 5; mainly 1 - 5	205°-255°; mainly 243°-255°	nearly parallel	1	clear sky	See text	
M23 Homog. terrain	Moree 23/11/83	11.34 & 13.22	13	79.5	3	180°, 360°	1.5-4.0; mainly 2.5-3.5	variable, 50°-140°	mainly perpendicular	4 parallel tracks at 1.5km from one another	2/8 Cu to 4/8 Cu	Mainly harvested wheat field and medium vegetation in uncultivated land;some green pasture land; and brown-black ploughed land;patches of forested land	Some short-lived rain showers occur near the observation site, and a brief shower occur over the end of one ground track at some stage, ahead of the aircraft run
M29 Homog. terrain	Moree 26/01/82	14.08 & 14.43	6	79.2	3	30°, 210°	1-2	variable, but mainly 60°	nearly parallel	1	1/8 Cu	Similar to M23	

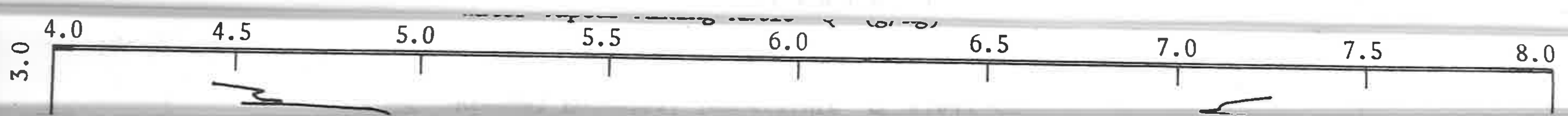

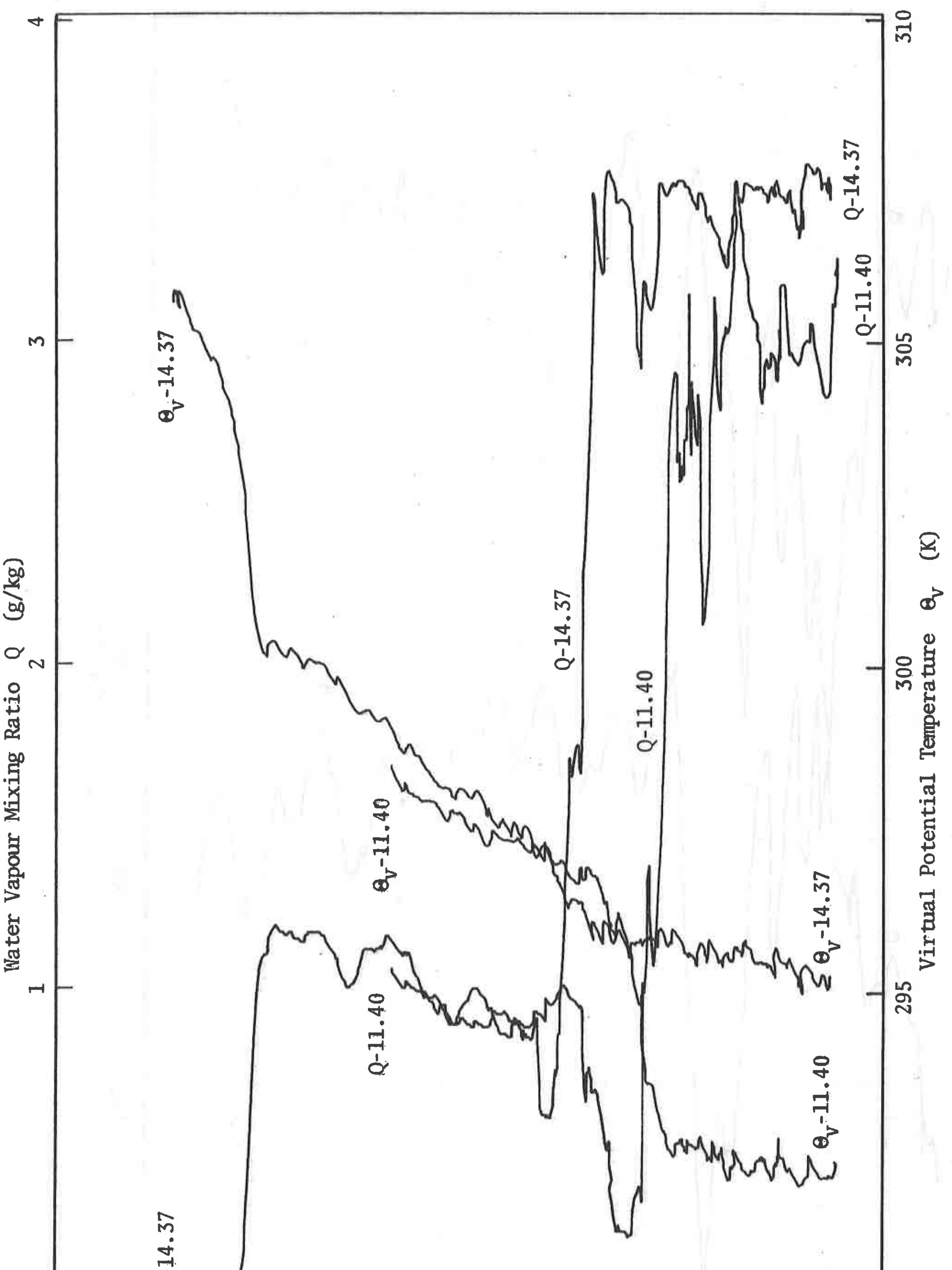
Water Vapour Mixing Ratio Q (g/kg)
0
1
2
3
4
Height above Ground Level (Callide Reservoir Level) z (km)
0.0
0.5
1.0
1.5
2.0
2.5
3.0
3.5
Virtual Potential Temperature θ_V (K)
290
295
300
305
310
Q-14.37
θ_V-14.37
Q-11.40
θ_V-11.40
Q-14.37
Q-11.40
θ_V-11.40
θ_V-14.37
Q-11.40
Q-14.37

Fig. 1a

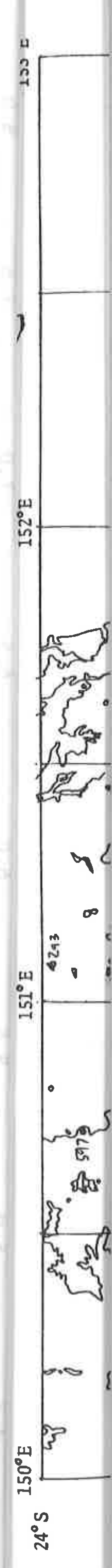
153°E
152°E
151°E
150°E
24°S

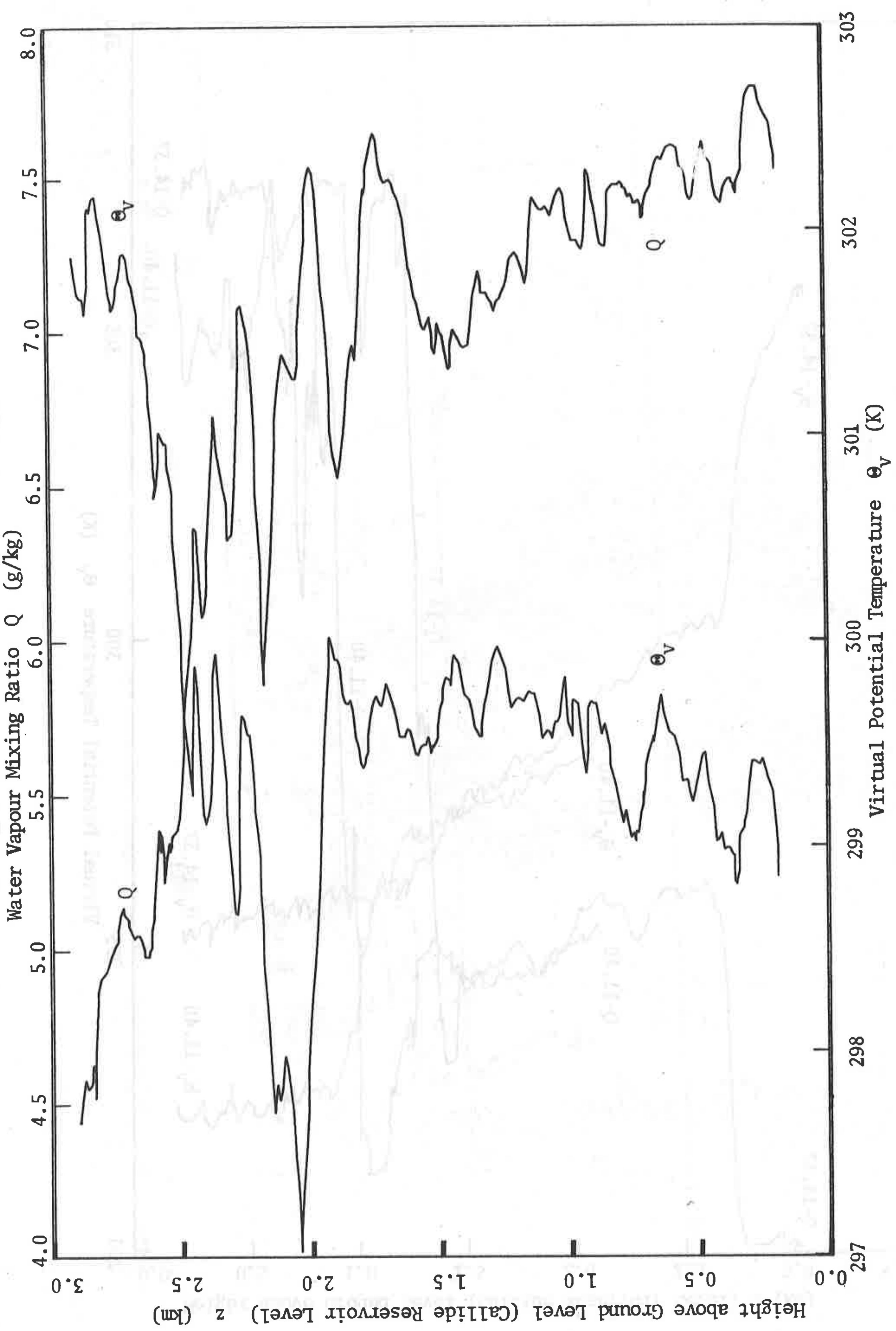
Water Vapour Mixing Ratio Q (g/kg)
4.0
4.5
5.0
5.5
6.0
6.5
7.0
7.5
8.0
Virtual Potential Temperature Θ_v (K)
297
298
299
300
301
302
303
Height above Ground Level (Callide Reservoir Level) z (km)
0.0
0.5
1.0
1.5
2.0
2.5
3.0
Q
Θ_v
Q
Θ_v

Fig. 1b

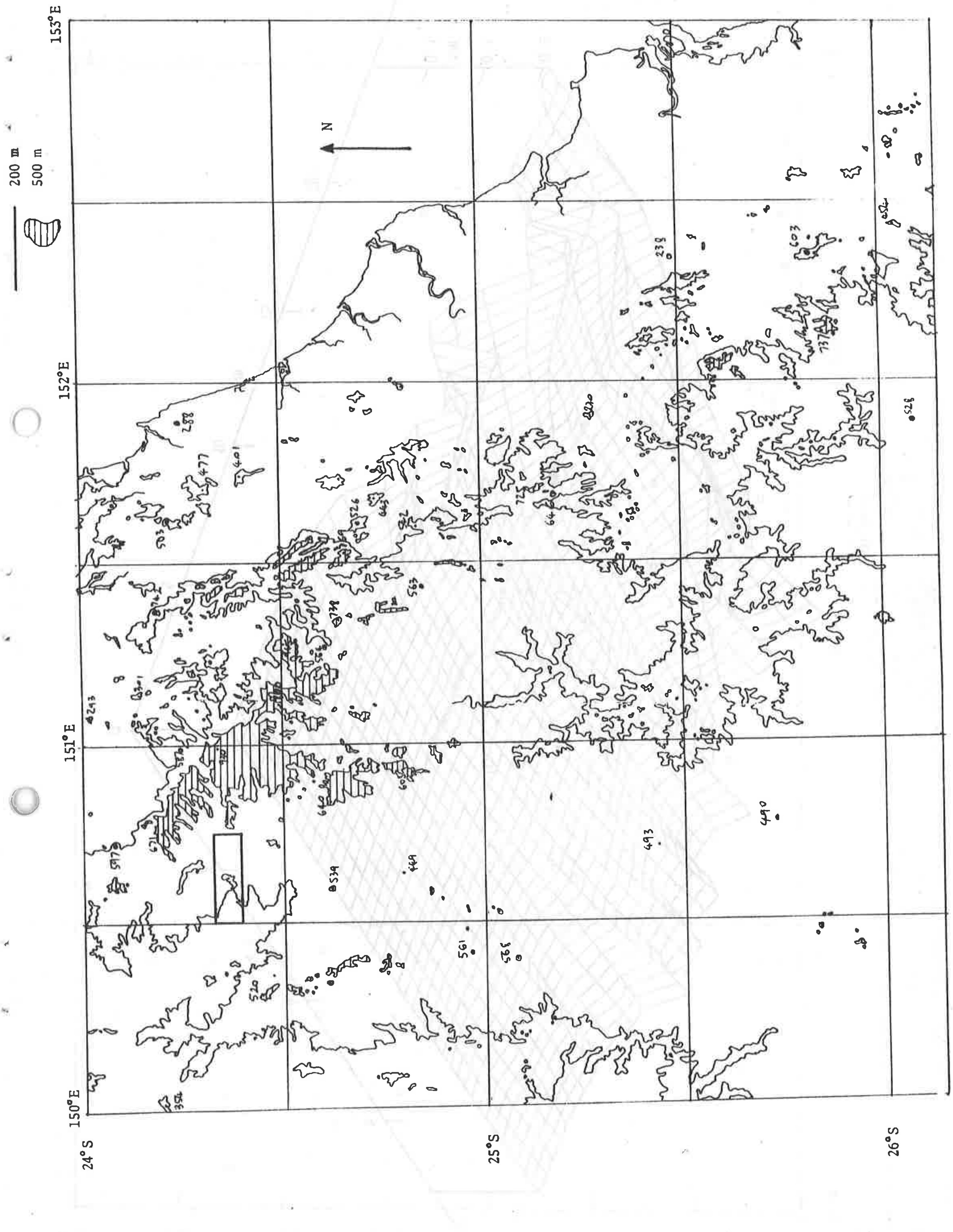
200 m
500 m
N
153°E
152°E
151°E
150°E
24°S
25°S
26°S
288
477
401
526
563
739
243
597
539
449
561
520
354
493
490
528
239
603

Fig. 2a

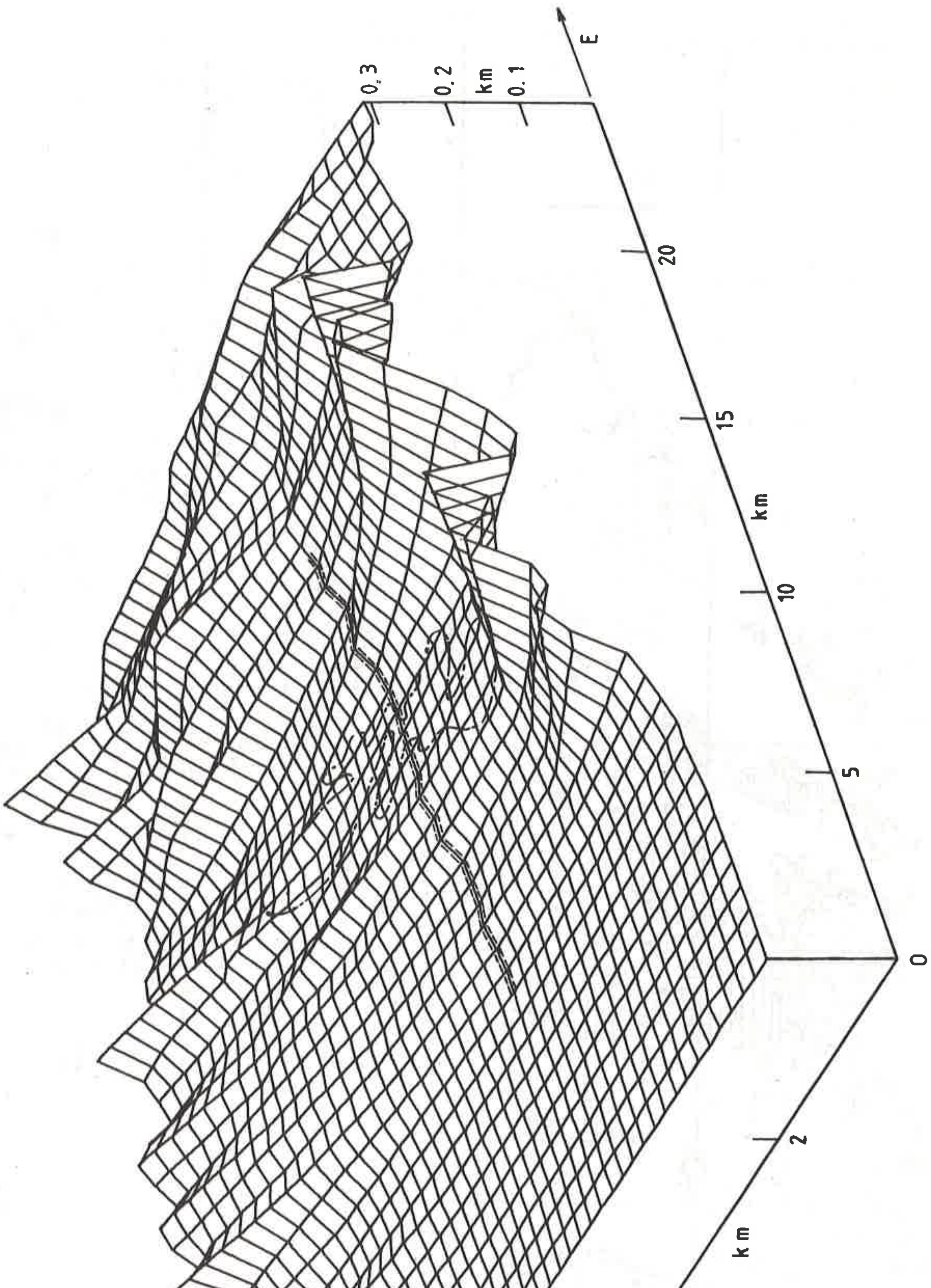

Fig. 2b

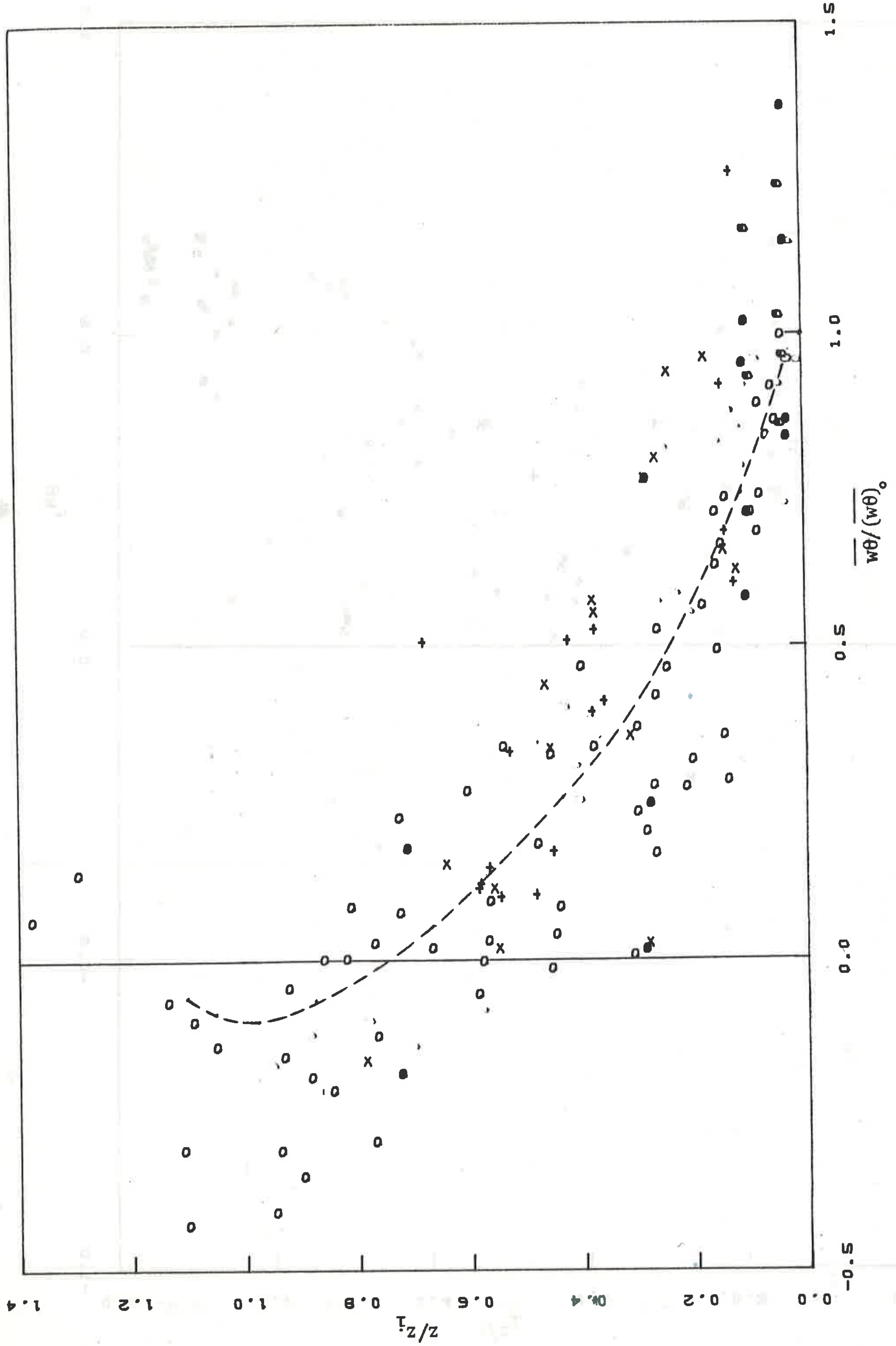
$\overline{w\theta}/(\overline{w\theta})_o$
-0.5
0.0
0.5
1.0
1.5
z/z_i
0.0
0.2
0.4
0.6
0.8
1.0
1.2
1.4

Fig. 3

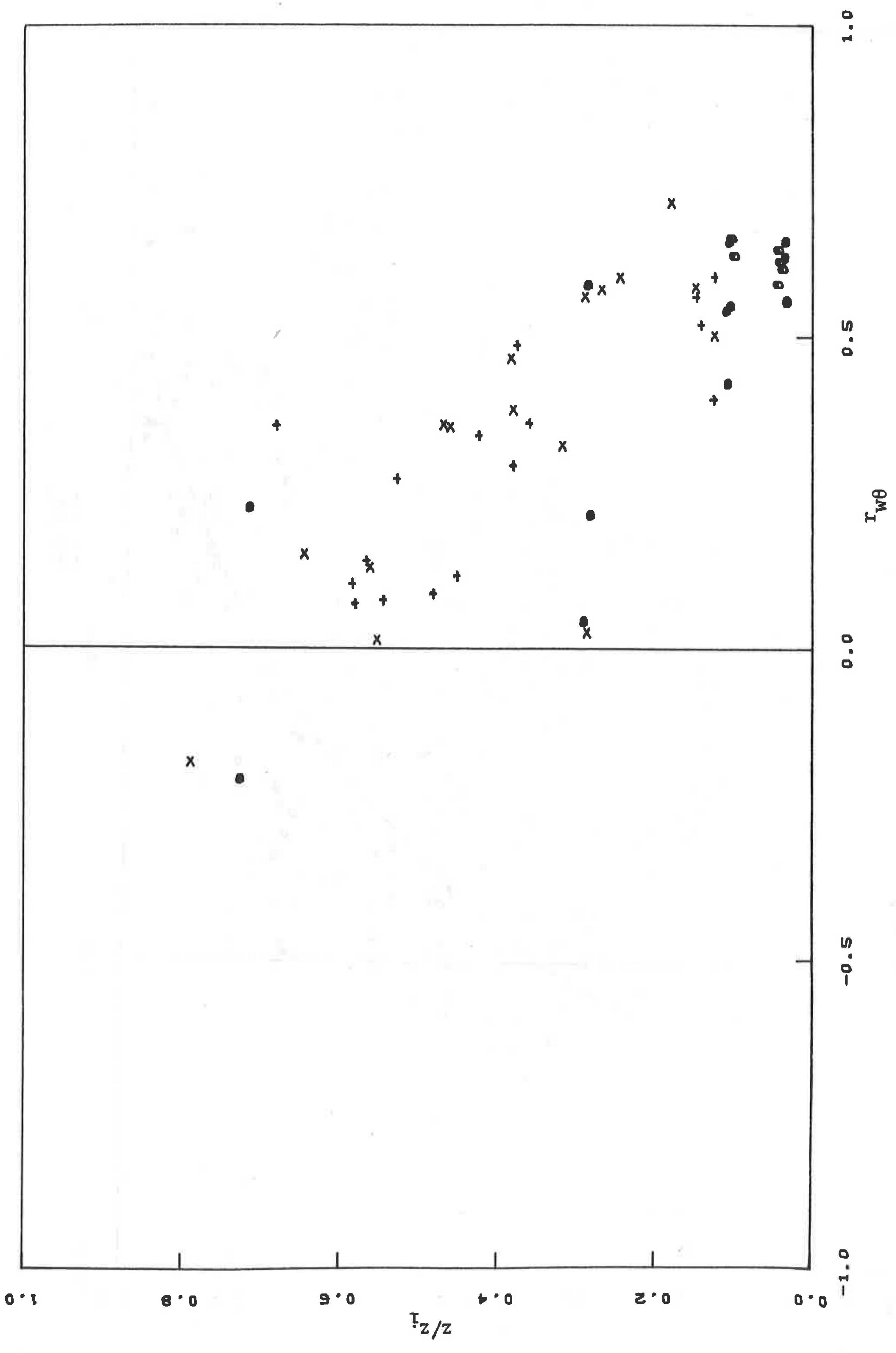

Fig. 4

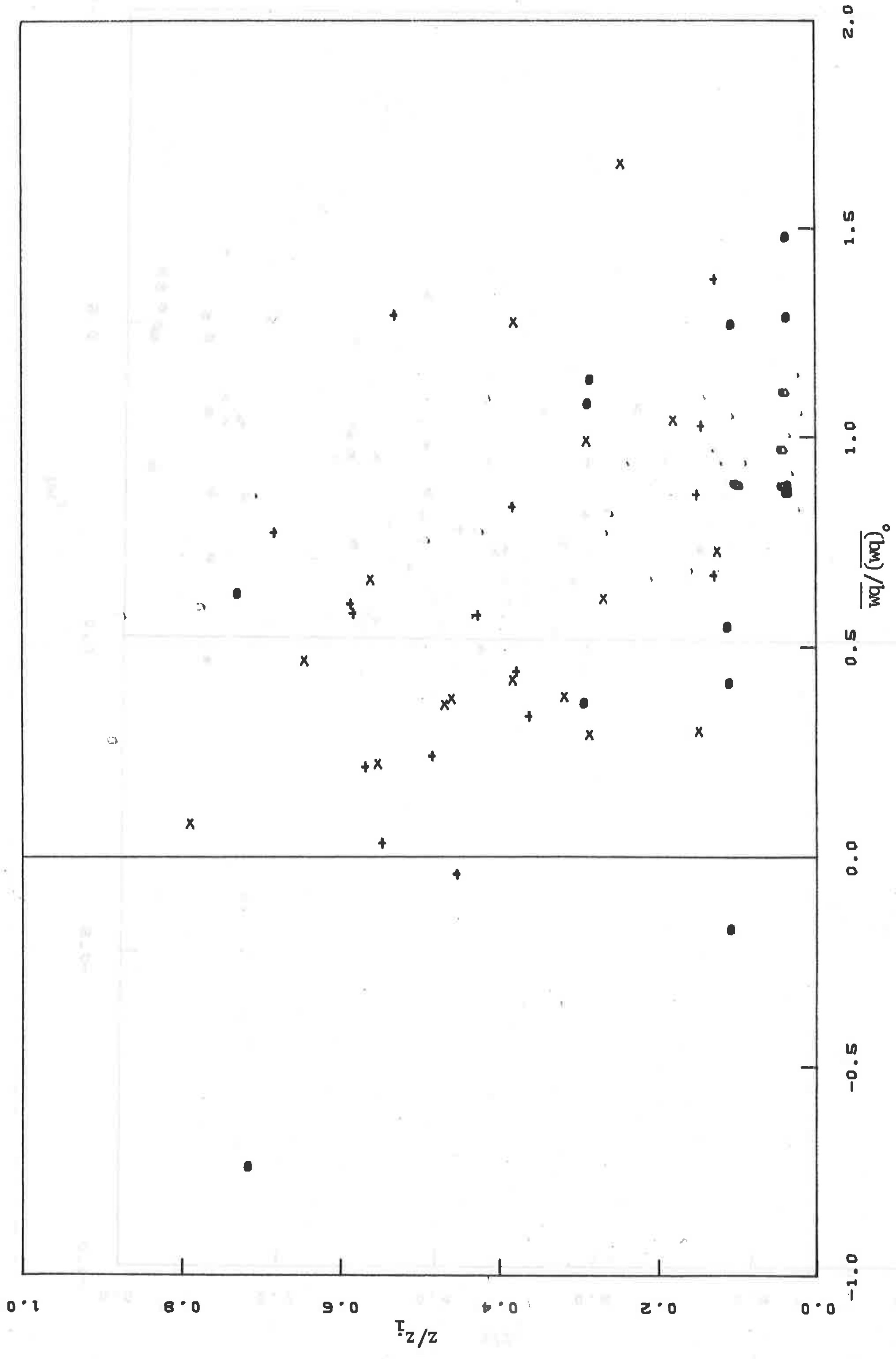
z/z_i
0.0
0.2
0.4
0.6
0.8
1.0
$\overline{wq}/(\overline{wq})_o$
-1.0
-0.5
0.0
0.5
1.0
1.5
2.0

Fig. 5

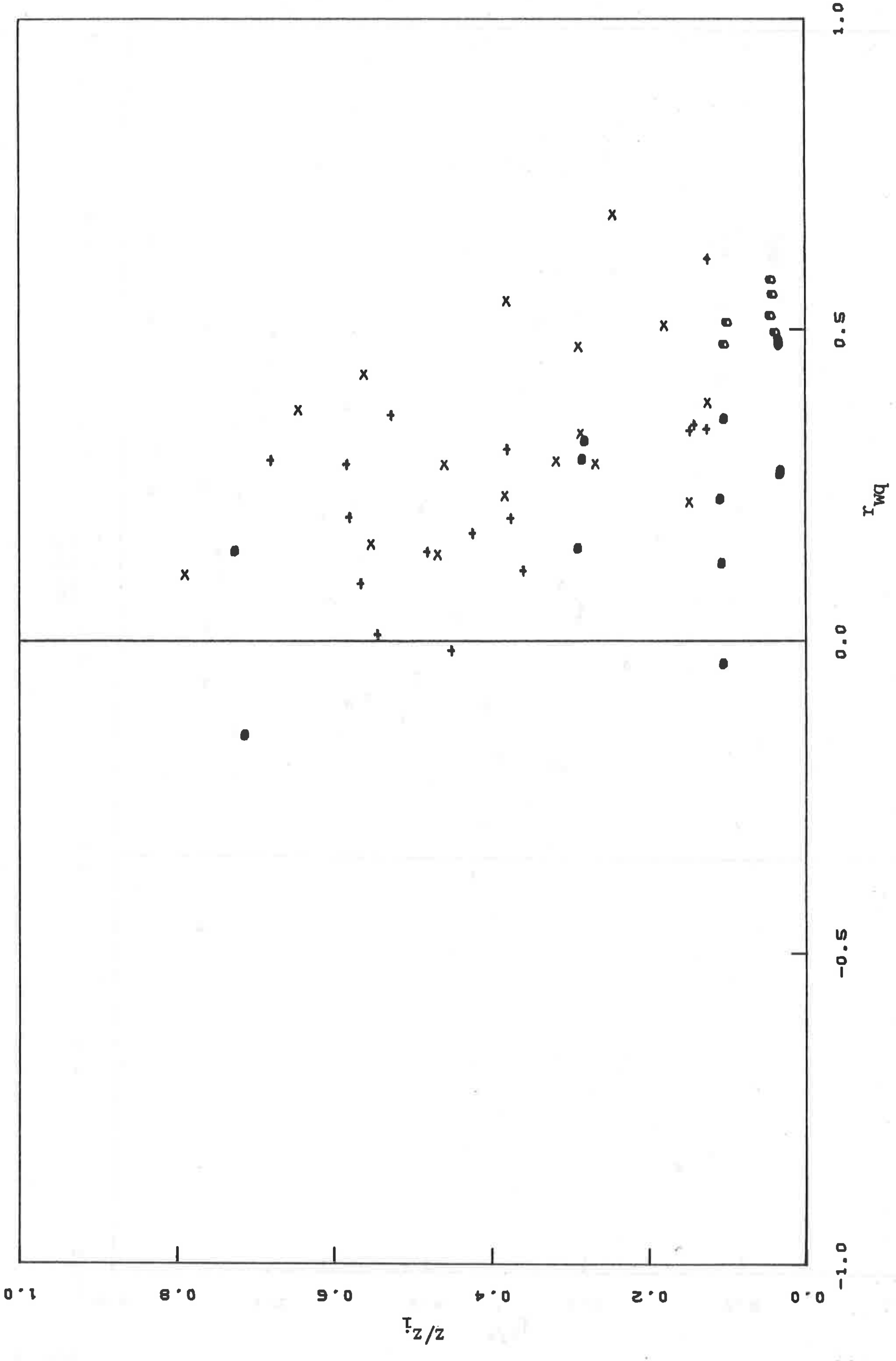

Fig. 6

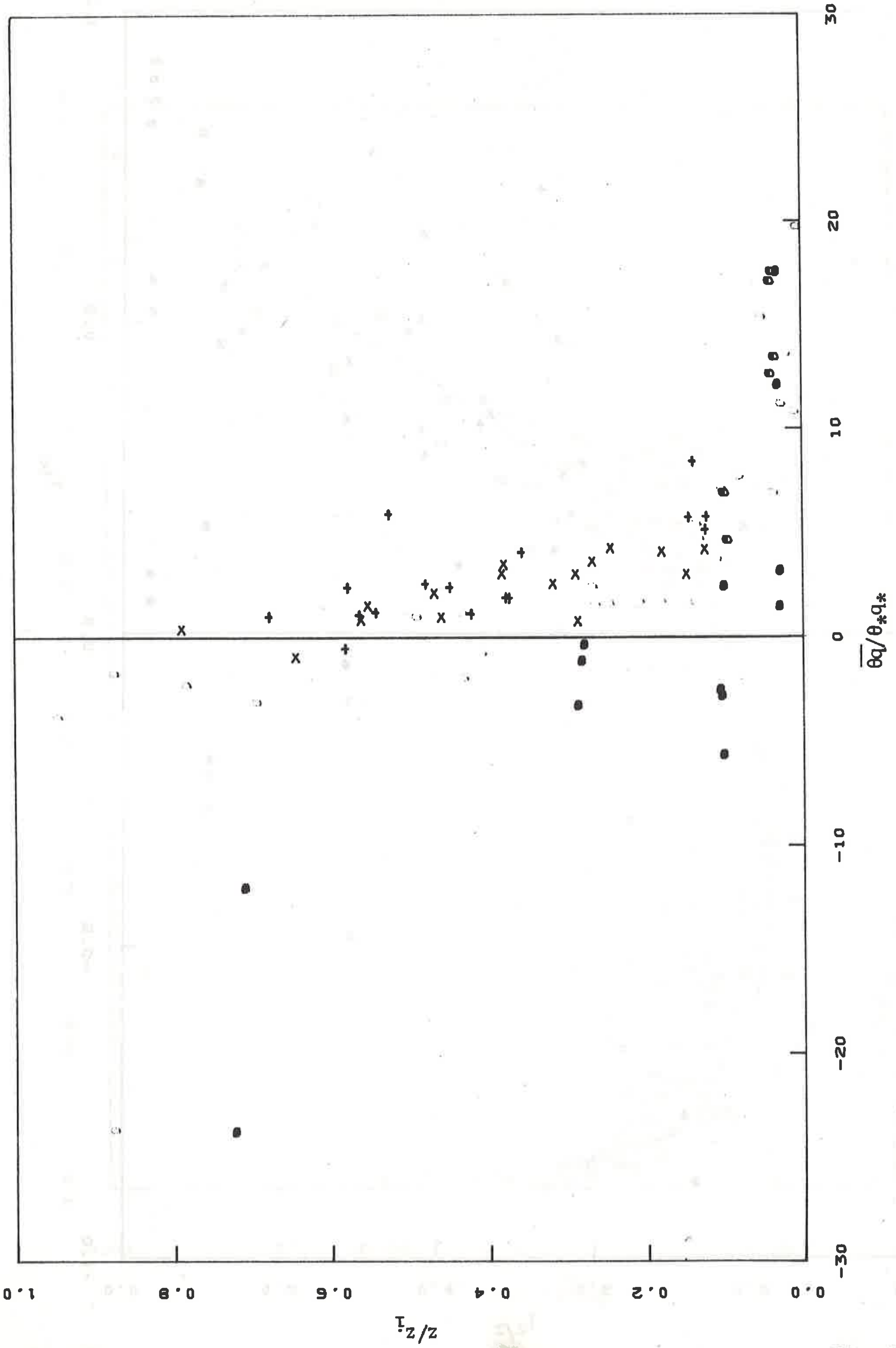

Fig. 7

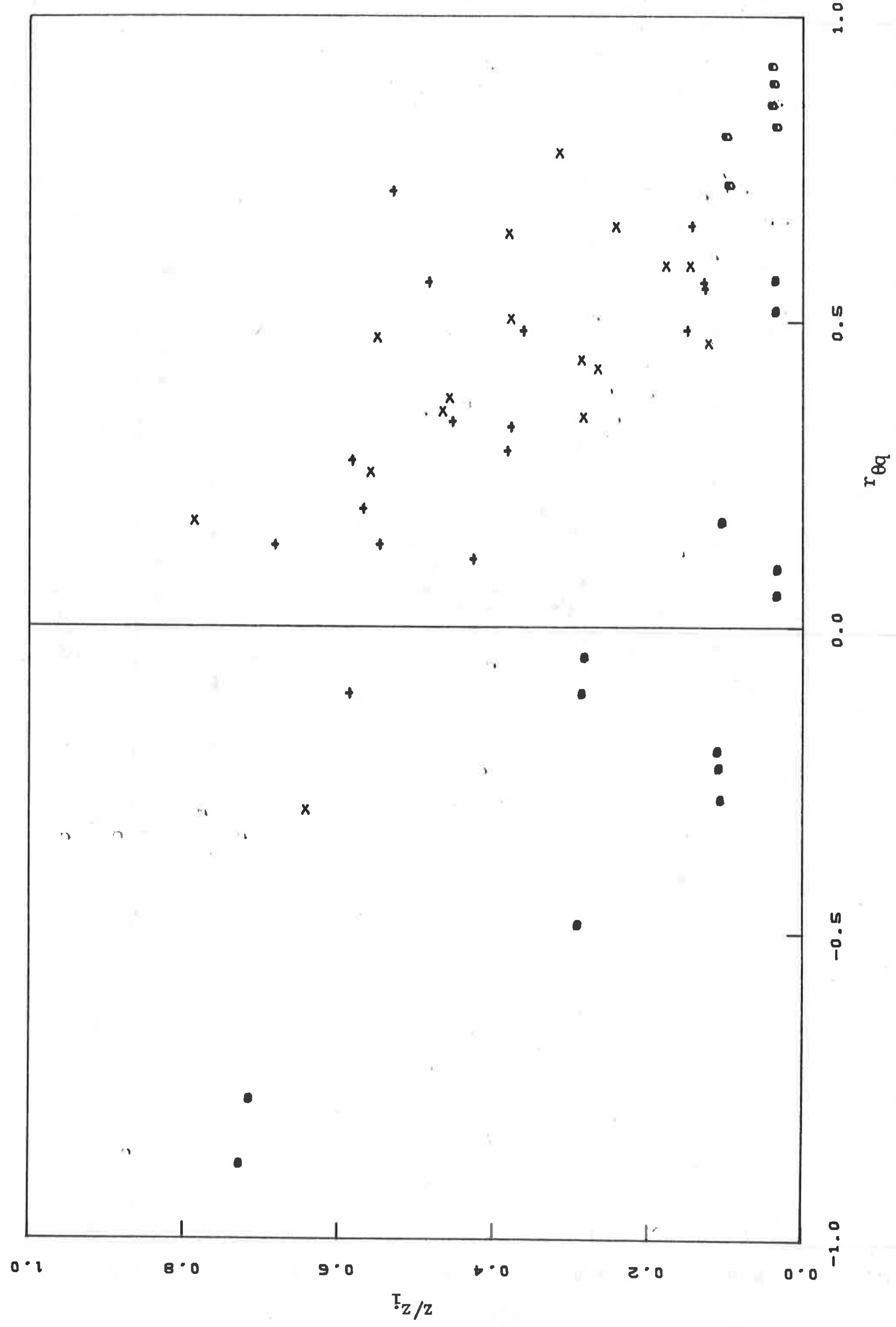

Fig. 8

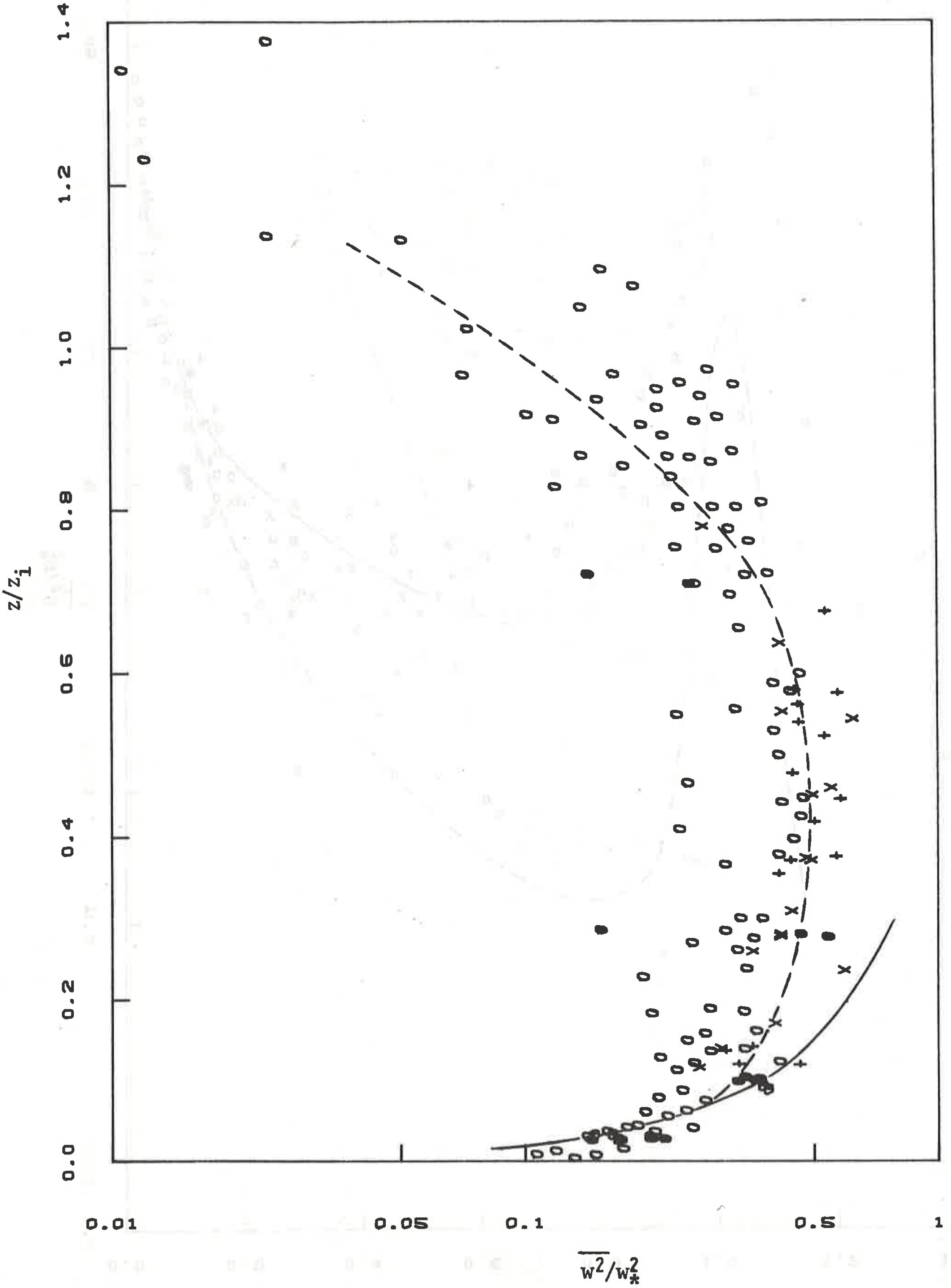

Fig. 9

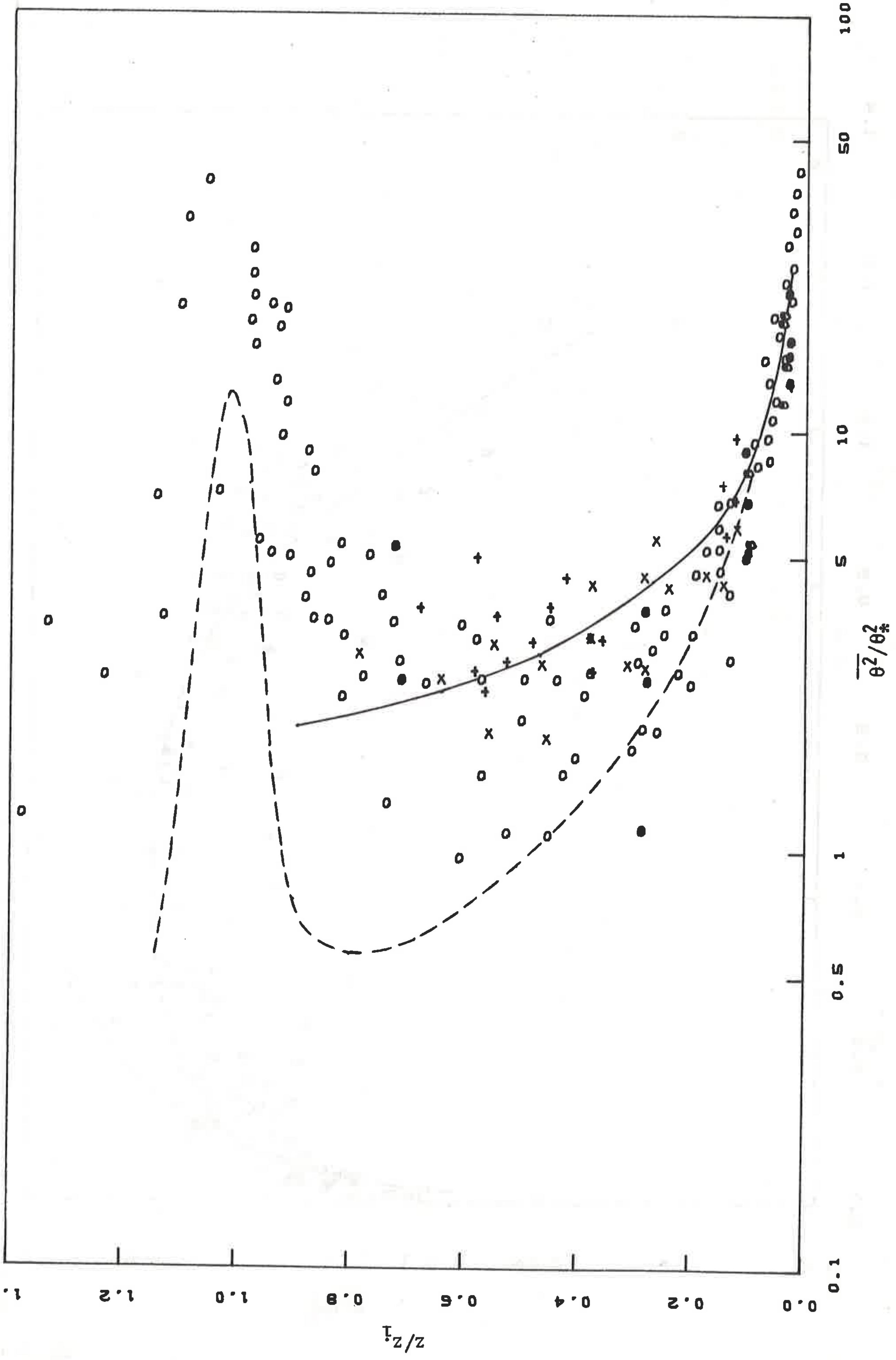
0.0
0.2
0.4
0.6
0.8
1.0
1.2
1.4
z/z_i
0.1
0.5
1
5
10
50
100
$\overline{\theta^2}/\theta_*^2$

Fig. 10

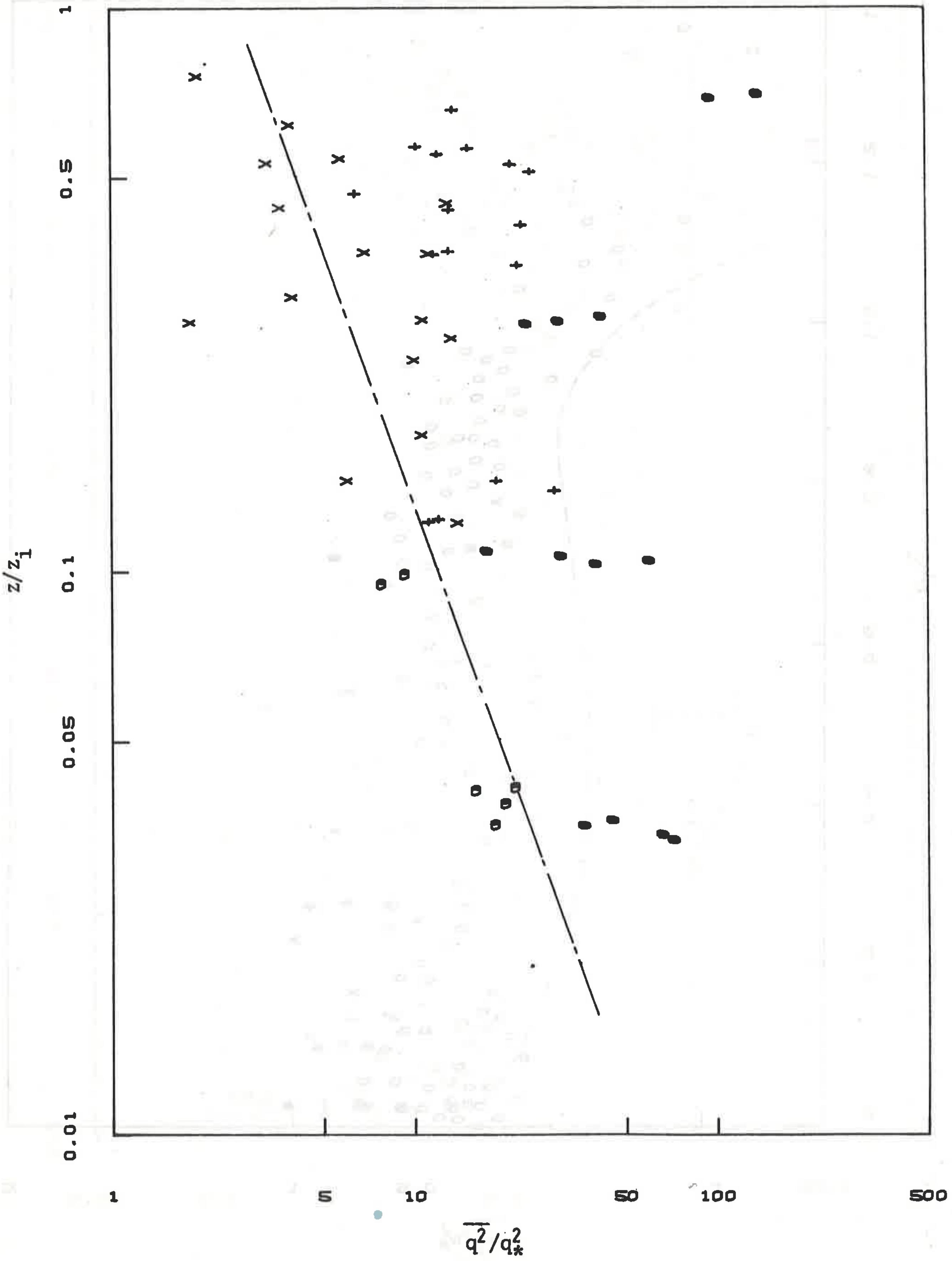

Fig. 11

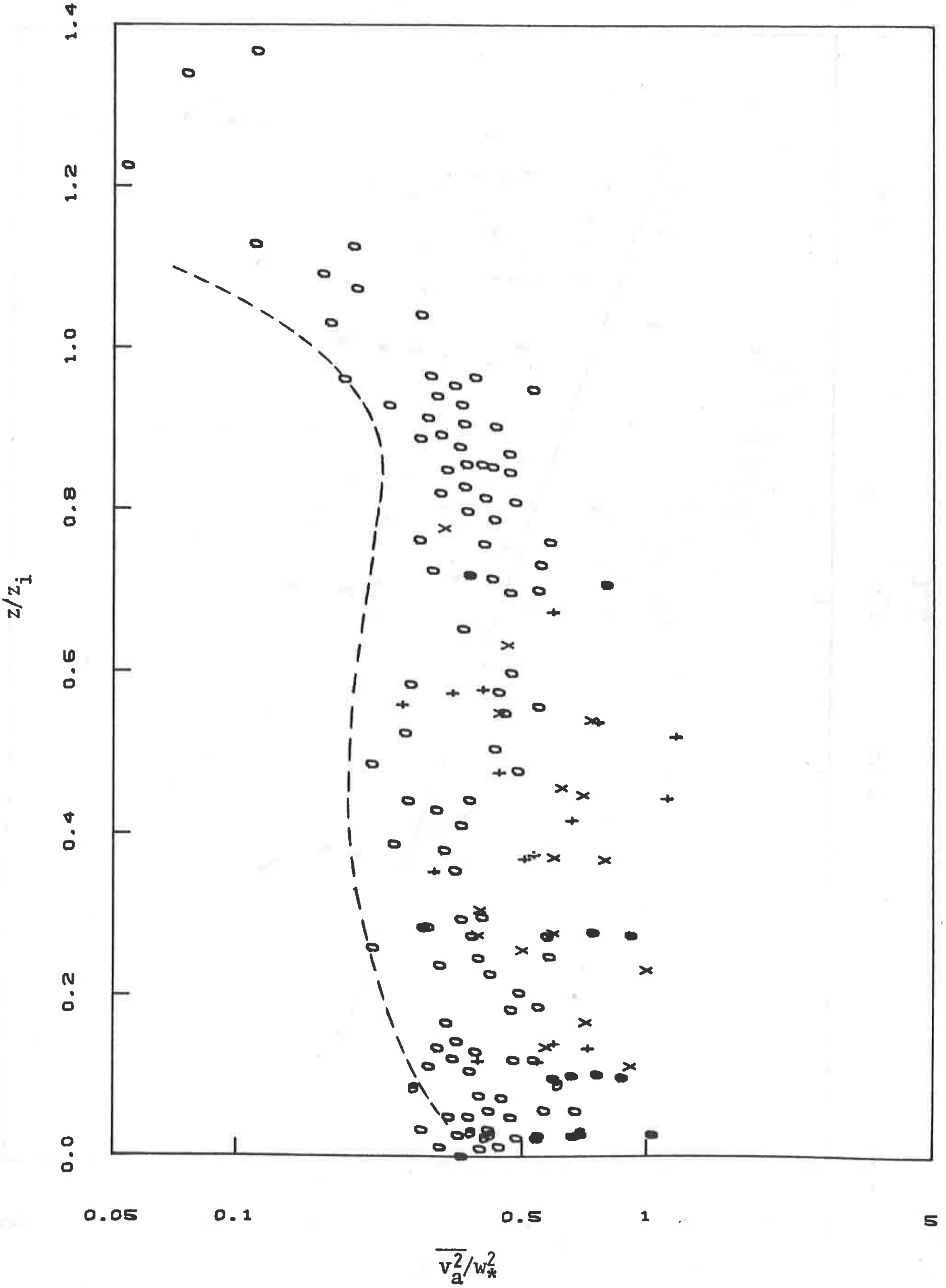

Fig. 12

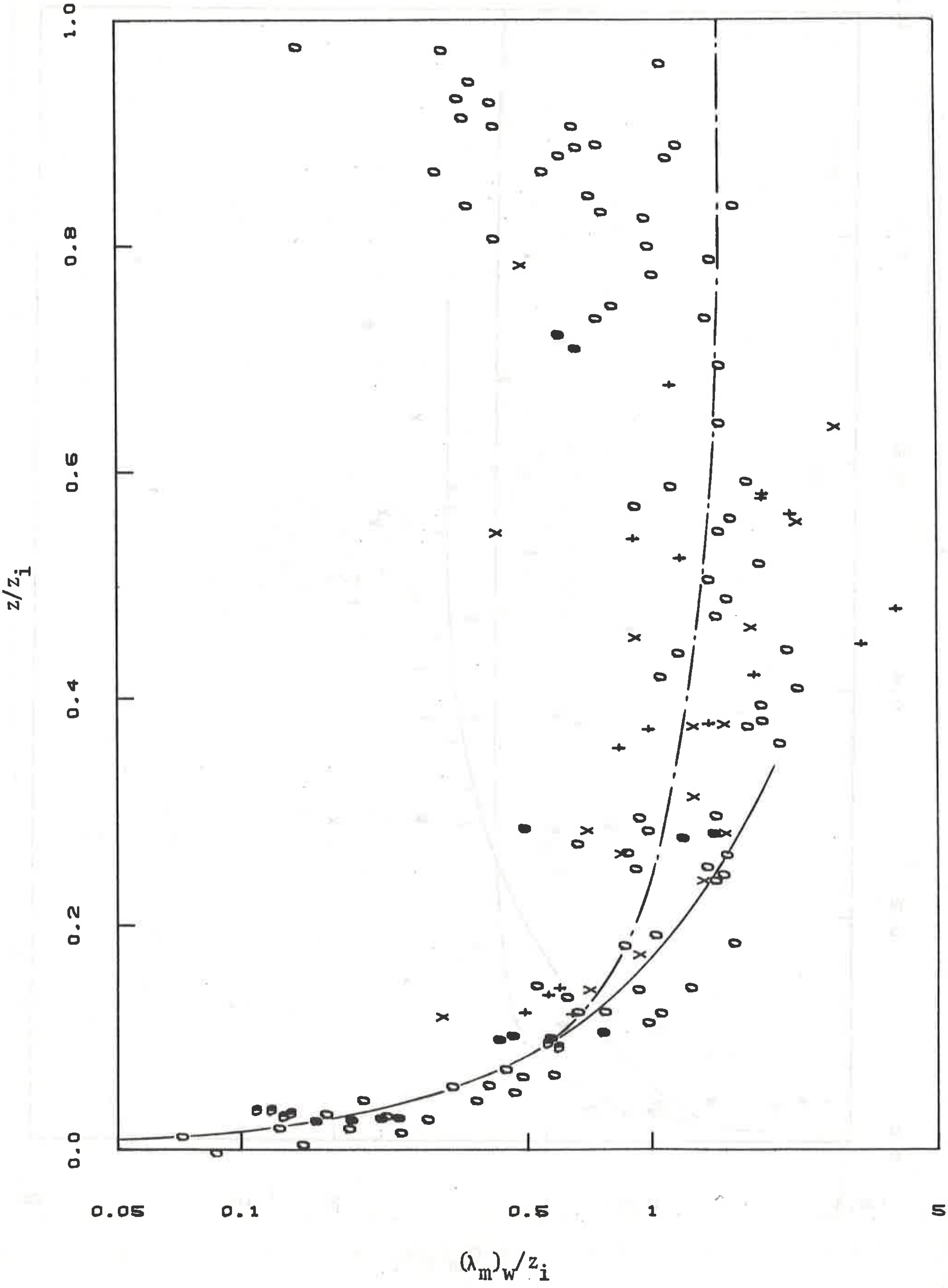

Fig. 13

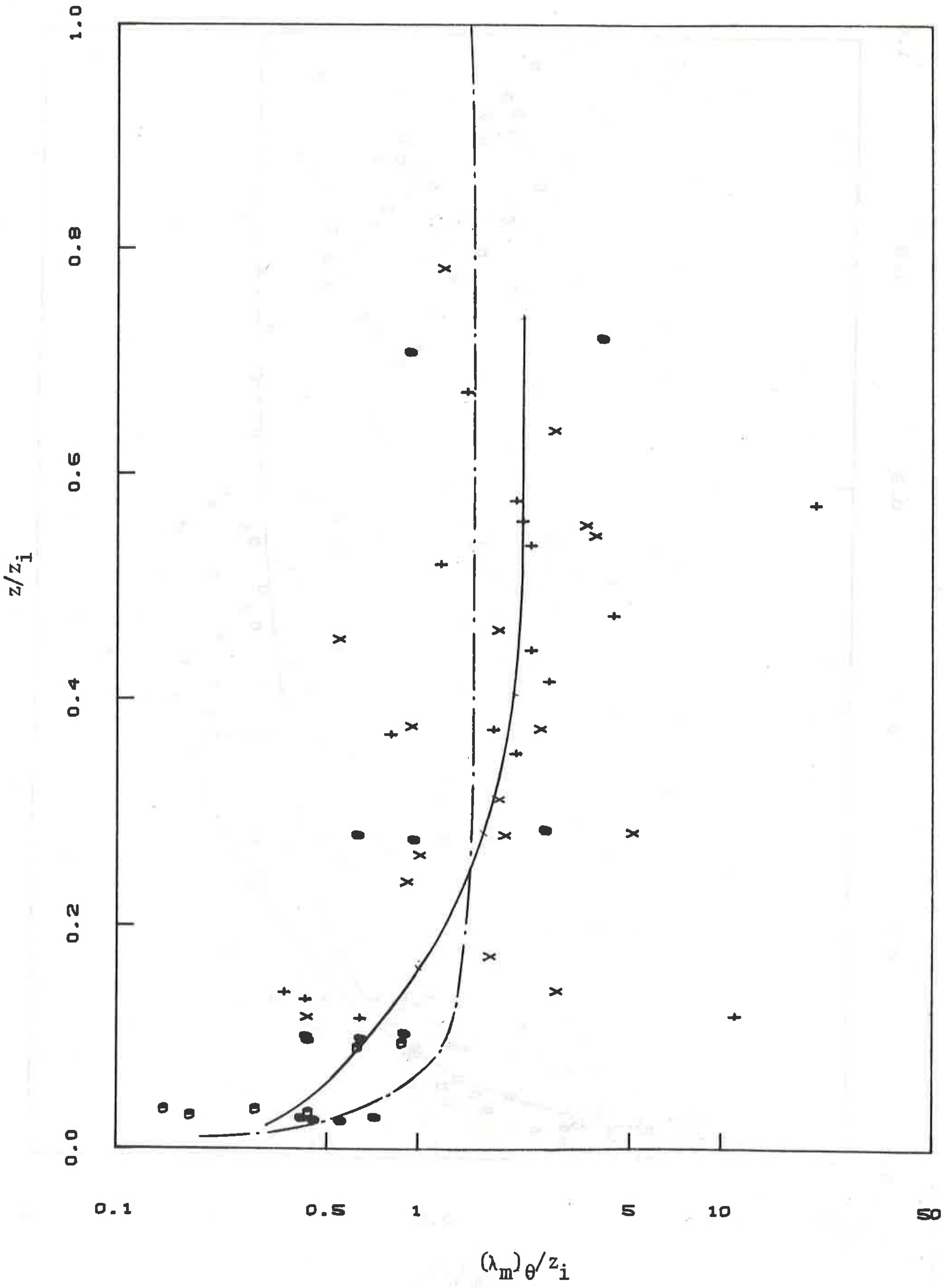

Fig. 14

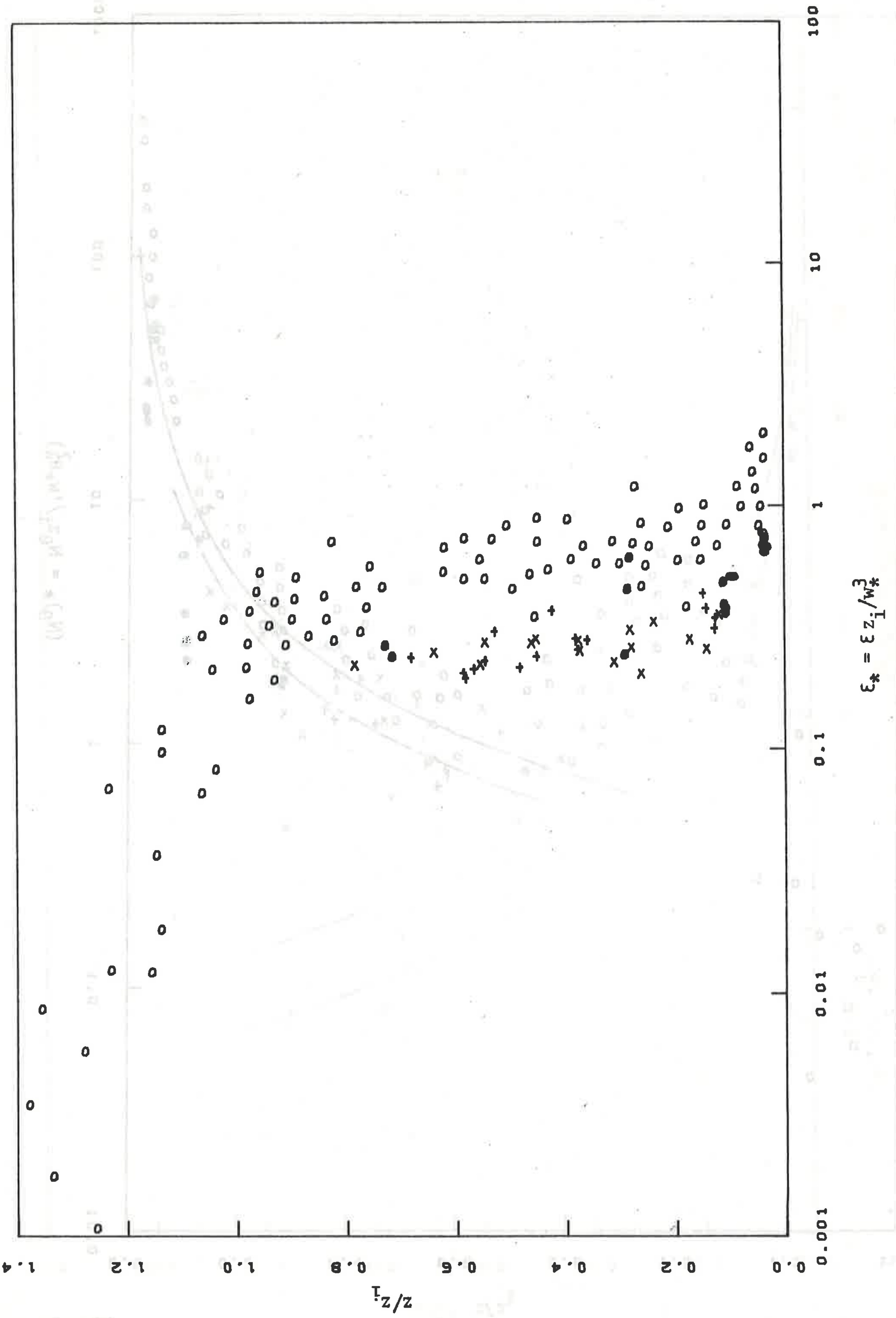

z/z$_i$
1.4
1.2
1.0
0.8
0.6
0.4
0.2
0.0
$\varepsilon_* = \varepsilon z_i/w_*^3$
0.001
0.01
0.1
1
10
100

Fig. 15

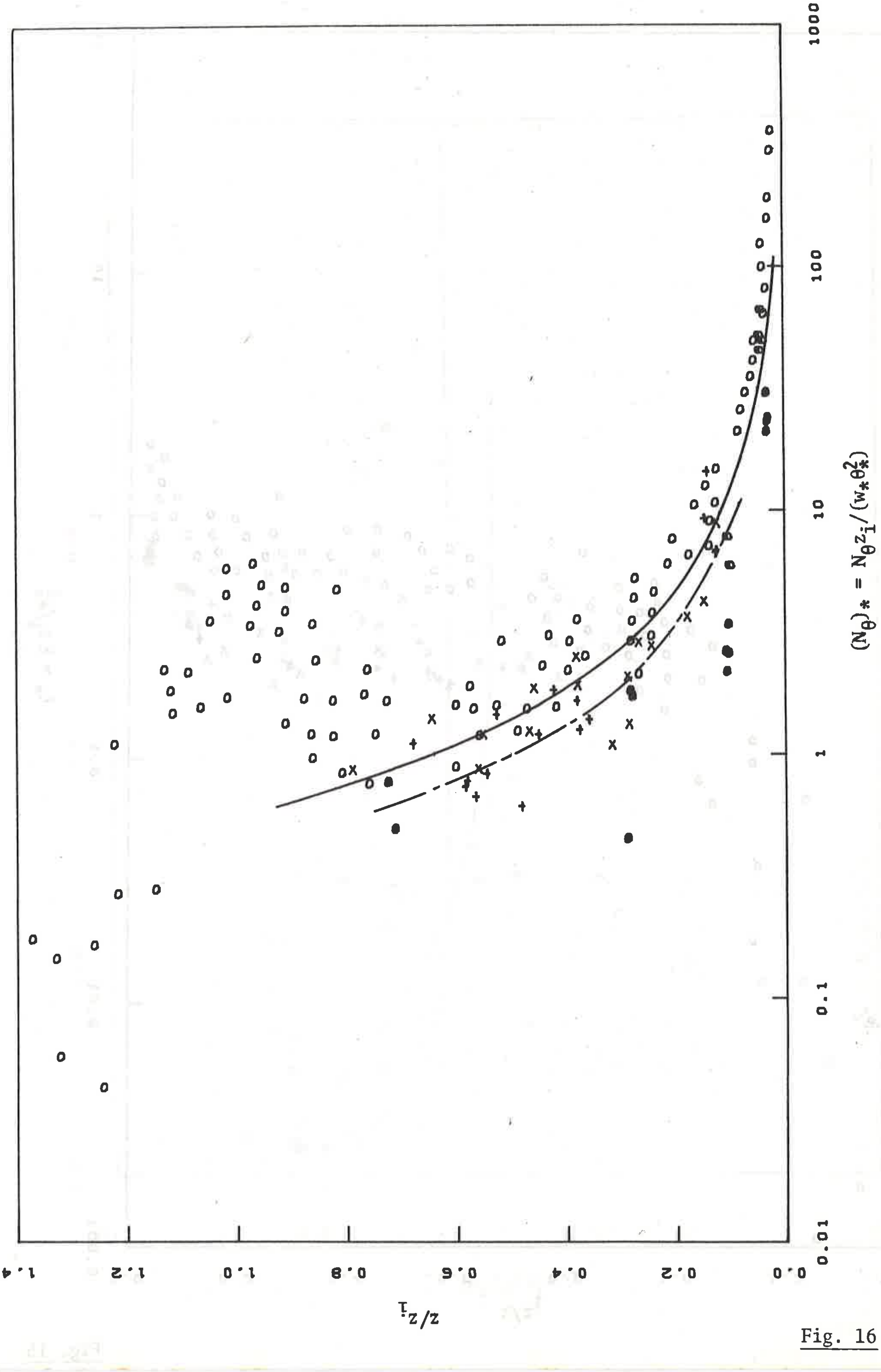

Fig. 16

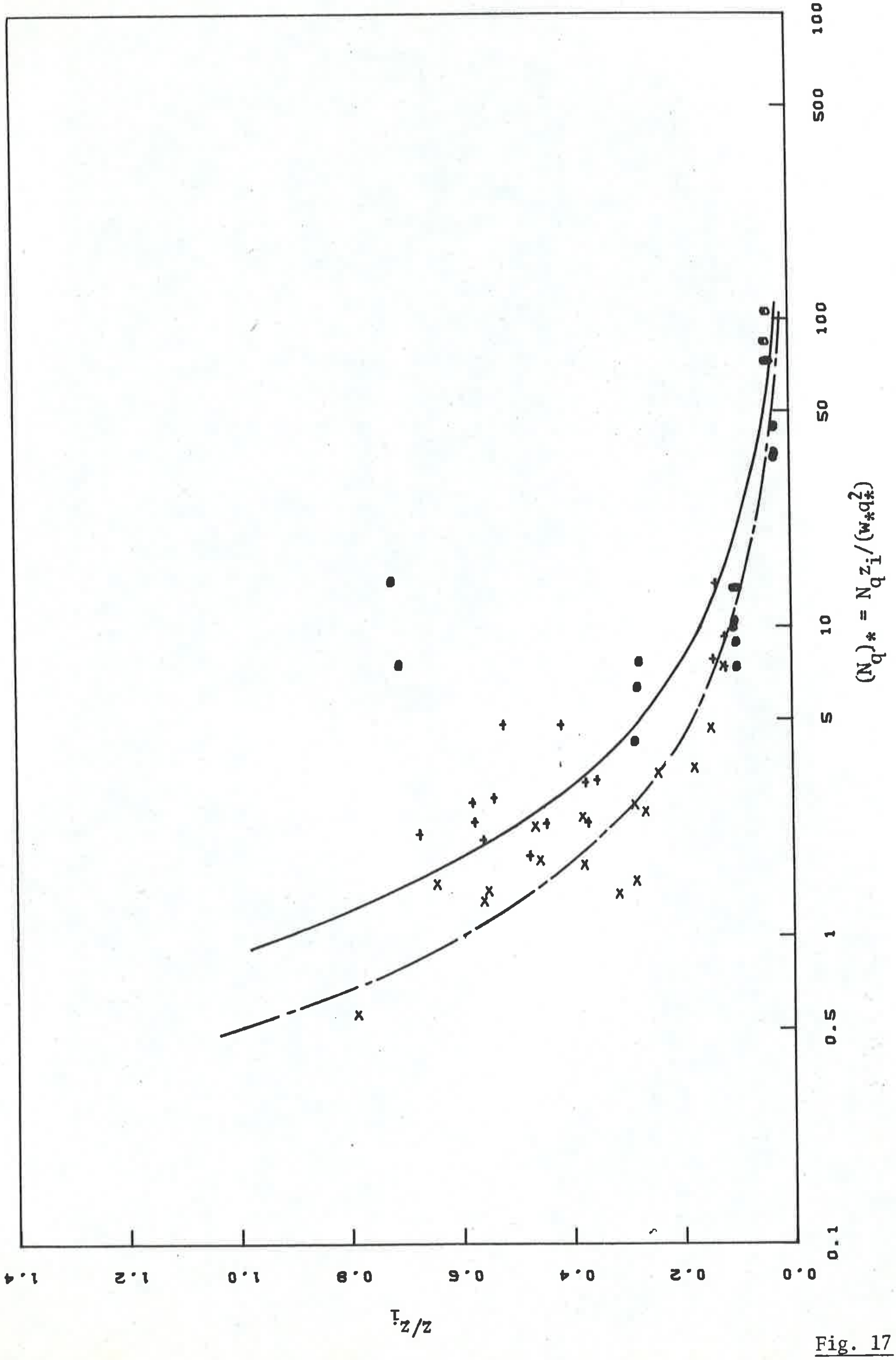

Fig. 17